1   **TITLE**

2   *The Italian contribution to the Synoptic Arctic Survey programme: the 2021 CASSANDRA cruise*
3   *(LB21) through the Greenland Sea Gyre along the 75°N transect*

4   **AUTHORS**

5   Manuel Bensi[1*], Giuseppe Civitarese[1], Diego Borme[1], Carmela Caroppo[2], Gabriella Caruso[3],
6   Federica Cerino[1], Franco Decembrini[3], Alessandra de Olazabal[1], Tommaso Diociauti[1], Michele
7   Giani[1], Vedrana Kovacevic[1], Martina Kralj[1], Angelina Lo Giudice[3], Giovanna Maimone[3], Marina
8   Monti[1], Maria Papale[3], Luisa Patrolecco[5], Elisa Putelli[1], Alessandro Ciro Rappazzo[3], Federica
9   Relitti[1], Carmen Rizzo[3,4], Francesca Spataro[5], Valentina Tirelli[1], Clara Turetta[6], Maurizio Azzaro[3]

11   [1] National Institute of Oceanography and Applied Geophysics, OGS, Trieste, Italy

12   [2] Water Research Institute, National Research Council, CNR-IRSA, Taranto, Italy

13   [3] Institute of Polar Sciences, National Research Council, CNR-ISP, Messina, Italy

14   [4] Stazione Zoologica Anton Dohrn, Sicily Marine Centre, SZN-SMC, Messina, Italy

15   [5] Institute of Polar Sciences, National Research Council, CNR-ISP, Rome, Italy

16   [6] Institute of Polar Sciences, National Research Council, CNR-ISP, Venice, Italy

17   *Correspondence to*: (mbensi@ogs.it)

18   **ABSTRACT**

19   In September 2021, as part of the Italian Arctic research programme, a multidisciplinary cruise
20   along the 75th parallel north through the Greenland Sea Gyre was conducted aboard the Italian
21   icebreaker Laura Bassi in the framework of the CASSANDRA project, which also contributed to
22   the Synoptic Arctic Survey (SAS) 2020/22. The cruise took place during the period of the lowest
23   summer sea ice extent ever measured. The data show strong horizontal gradients with temperatures
24   between 1.5 °C and 9.0 °C and salinity between 30 and 35. Warm and salty Atlantic Water (AW, θ
25   > 3.0 °C, S around 35) dominates on the eastern side of the transect in the upper 500 m with surface
26   temperatures of 4.5–9.0 °C, while Polar Water (PW, θ < 0 °C, S < 33) occupies the surface layer
27   (50–80 m) in the west. The intermediate layer (100–500 m) consists of mixed water, and below 500
28   m the deep water of the Greenland Sea and the Norwegian Sea predominates. The oxygen
29   enrichment is higher in the intermediate layers, while the values in deep layers and western regions
30   are lower (< 300 µmol kg^{-1}). A stratified upper layer (30–50 m deep) with low surface nutrients,
31   especially nitrate, is observed, while an accumulation of silicate occurs in deep water masses. The
32   surface water in the eastern part of the transect has high pH$_T$ and total alkalinity values due to
33   photosynthesis and the presence of salty AW, while the fresh PW in the west has a lower alkalinity.
34   Respiratory activity and organic matter concentrations (particulate/dissolved organic carbon) vary
35   horizontally at the surface, decrease with depth, and increase slightly near the seafloor. A west-east
36   gradient is also observed for δ^{18}O and δD, with the ratios indicating the influence of freshwater at
37   the surface near the Greenland coast. The abundance of prokaryotes decreases from the photic zone

38 (< 100 m depth) to the sea floor. Carbohydrates and carboxylic acids are identified as well-utilised
39 polymers at every station and in every layer. Overall, the microbial enzyme patterns show a decrease
40 from the surface to deeper layers, with some hotspots of metabolic activity at 20-40 m and in the
41 aphotic layer. The enzyme patterns vary spatially, with activity peaks at the ends and in the middle
42 of the transect. Phytoplankton biomass, expressed as chlorophyll-a, varies across the transect, with
43 higher values at the westernmost and easternmost stations. The micro-phytoplankton fraction
44 dominates in PW, while the nano-phytoplankton fraction predominates in AW, even at the interface
45 between the two water masses. Data of phytoplankton communities show low abundances and a
46 dominance of nano-sized organisms, with diatoms being more abundant in the western part.
47 Microzooplankton represents an important fraction of the planktonic community in this area, with
48 tintinnids being the most important groups along the transect. Micrometazoans and aloricate ciliates
49 are more abundant in the AW, resulting in higher biomass values at the eastern stations. Copepods
50 are the most abundant mesozooplanktonic taxon both at the surface and in the upper 100 m water
51 layer (97% and 94% of total mesozooplankton abundance, respectively), mainly represented by the
52 genus *Calanus*.

53 The data are publicly available at the Italian Arctic Data Centre (IADC), see section Data
54 availability.

1   INTRODUCTION

56 The Greenland Sea, in the north Atlantic, is a region of deep ocean convection that contributes to
57 the Atlantic Meridional Overturning Circulation (AMOC) and the exchange of water masses
58 between the Atlantic and Arctic Oceans. Its sensitivity to climate change remains uncertain, as the
59 ecosystems of the subarctic Atlantic are particularly sensitive to global warming (Whitt, 2023). In
60 fact, the Greenland Sea serves also as a hub for heat, salts, nutrients, carbon, and organisms between
61 the Arctic, subarctic, and lower latitudes. Arctic and subarctic regions have experienced warming
62 twice as fast as global warming over the past 50 years (Rantanen et al., 2022). This has led to
63 significant environmental changes, including increasing wetness, reduced sea ice thickness and
64 coverage, changes in snow cover, thawing of permafrost, and melting of the Greenland ice sheet
65 (Carmack et al., 2015; Polyakov et al., 2017, 2023; Babb et al., 2023). These changes have created
66 a positive feedback loop known as "Arctic amplification" which is likely to intensify in the future.
67 Despite its crucial role in the global climate system, the Arctic Ocean remains poorly understood
68 due to its remote location, harsh weather, and seasonal ice cover. The Arctic Ocean receives heat
69 through the inflow of Atlantic Water (AW, with Temperature (T) > 0 °C). AW flows northward
70 transported by the Norwegian Atlantic Current (NAC) and the West Spitsbergen Current (WSC)
71 along the eastern slope of the North Atlantic and crosses the Greenland Sea and Fram Strait, where
72 it is partly deflected by the local circulation (Fig. 1). On the other hand, the Arctic outflow of Polar
73 Water (PW, T < 0 °C), together with the sea ice export from the Arctic, is driven by the East
74 Greenland Current (EGC, Chatterjee et al., 2018). Greenland freshwater flux shows a large seasonal
75 variation, with peaks in July (4-6 times higher than in winter), but also consistent increase since the
76 2000s (Dukhovskoy et al., 2019). Changes in annual and multi-year sea ice trends are also an
77 important factor to consider when analysing the physical and biogeochemical conditions in the
78 Greenland Sea. Sea ice extent and thickness in the Arctic regions have continuously decreased over
79 the last four decades, and significant changes have also been observed in the Fram Strait since 2015
80 (de Steur et al., 2023). Since 2020, however, sea ice extent in the Fram Strait and marginal seas has

81 shown a slight recovery in seasonal winter maxima (Onarheim et al., 2024). Open-ocean convection
82 also occurs in the Greenland Sea during winter seasons. It is thought to represent a significant
83 proportion of dense water production for the regions, even though a large variability in this process
84 has been observed in recent decades, including changes in the depth of convection (Simpkins, 2019;
85 Brakstad et al., 2019). Overall, the predominant atmospheric conditions over the Arctic are
86 characterised by the presence of high pressure (i.e., Polar High) over the western Arctic and low
87 pressure over the Siberian region, which trigger the main anticyclonic wind regime. However, after
88 2007 a secondary dipole, characterised by higher sea level pressure over the Beaufort Gyre and the
89 Canadian Archipelago along with lower sea level pressure over the Siberian Arctic, became
90 dominantly positive, favouring reduced flows into the Arctic through the Fram Strait along with
91 enhanced inflows through the Barents Sea Opening (Polyakov et al., 2023). Consequently, from
92 2007 to 2021, the predominant cyclonic atmospheric regime over the Arctic Ocean pushed large
93 amounts of freshwater from the Siberian shelves into the Beaufort Gyre (Polyakov et al., 2023).

94 The cyclonic Greenland Sea Gyre (GSG) in the central Greenland Sea, which is mainly driven by
95 large-scale cyclonic winds, contributes to the regulation of the inflow and outflow of AW and PW
96 between the Atlantic and Arctic Oceans (Chatterjee et al., 2018). The GSG, and the North Atlantic
97 subpolar gyre (SPG), south of Iceland, have large implications for the large-scale changes in the
98 subpolar and polar marine environment. A strong GSG triggers a northwestward shift of the
99 subpolar front, which intensifies the poleward transport of Atlantic water towards the Fram Strait,
100 Barents Sea and Arctic Ocean (Chatterjee et al., 2018). In contrast, a weak phase (i.e., a negative
101 index, see Fan et al., 2023) in the SPG enables the northward expansion of subtropical warm and
102 saline waters, while a strong SPG feeds cold and fresh subpolar waters into the Atlantic inflow.

103

104

105
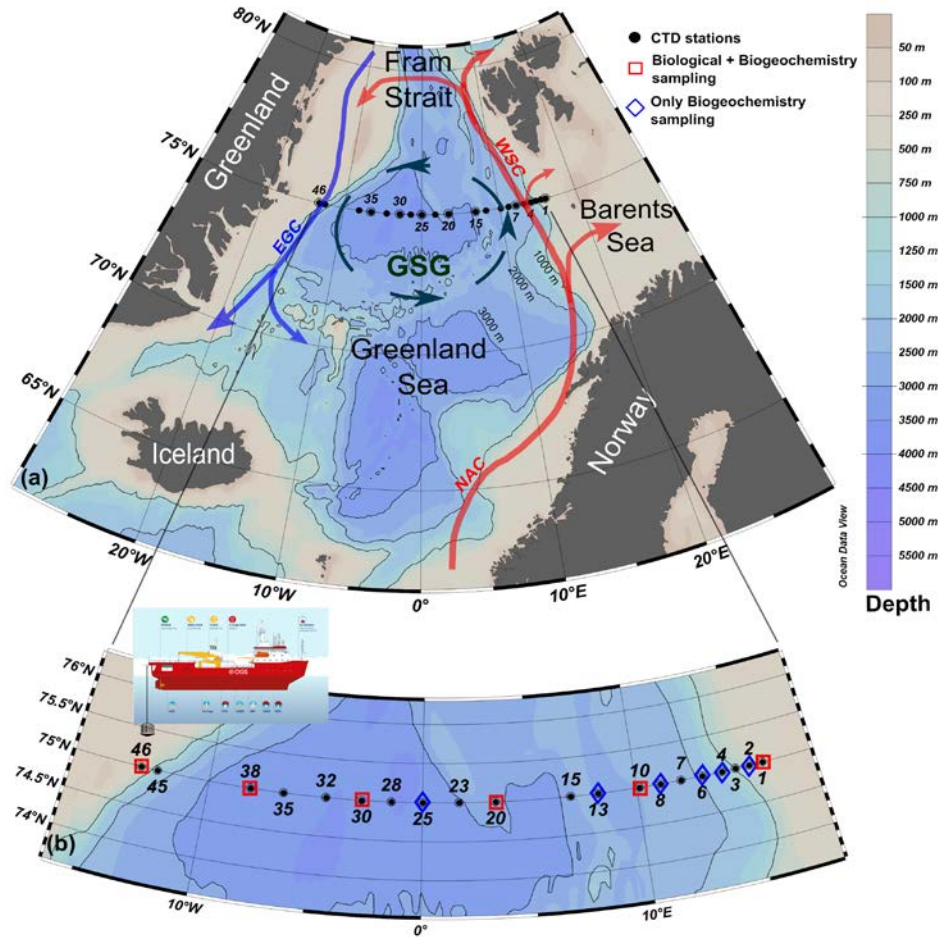
Figure 1 - **(a)** Schematic of the general circulation in the Greenland Sea (**GSG**-Greenland Sea Gyre; **WSC**-West Spitsbergen Current; **EGC**-East Greenland Current; **NAC-** Norwegian Atlantic Current). **(b)** Distribution of hydrological (CTD) stations conducted during the LB21 CASSANDRA cruise (29 August -14 September 2021) with the positions of the physical (black dots), biogeochemical and biological stations (blue and red symbols).

A time lag of 3-5 years is expected for the thermohaline anomalies to propagate in the Nordic seas (Fan et al., 2023) from the sub polar regions. In other words: while the GSG regulates the AW inflow into the Arctic, the SPG modulates the proportion of subtropical and subpolar waters moving at high latitudes. Wind forcing and heat loss combine to drive the full variability of the flow and water mass transformations in the region (Smedsrud et al., 2022).

The anomalous inflow of AW from the Nordic seas and the subpolar regions is referred to a process called Atlantification, which has various direct and indirect effects on the Arctic environment. This process has intensified since the 2000s, leading to, among other effects, increasing anomalies in temperature and salinity in the upper layer, a reduction in sea ice cover, reduced stratification of the upper ocean, increased primary production and a shift of the summer bloom to earlier periods, changes in the phenology, distribution and community composition of zooplankton, and spreading of subarctic species (Polyakov et al., 2017; Ingvaldsen et al., 2021; Csapò et al., 2021). Microbial communities are also affected by the co-occurrence of Atlantification and Arctic amplification, as pointed out by recent observations (Ahme et al., 2023; Priest et al., 2023). Microorganisms are pivotal drivers in all the earth ecosystems, as primary degraders of organic matter and main players in nutrient cycling. They are thus particularly sensitive to the external environmental conditions and

as such, play a role of optimal sentinels of global changes and trends (Caruso et al., 2016). Distinct bacterial communities have been reported between Atlantic- and Arctic-derived waters (Carter-Gates et al., 2020), and a direct effect of organic matter dissolution from the sea ice on the microbial diversity has been demonstrated, by documenting the occurrence of diverse bacterial assemblages between sea-ice and seawater (Yergeau et al., 2017). The Greenland Sea, like other Nordic Seas, is a sink for atmospheric CO_2 during the year (Skjelvan et al., 2005). The annual flux of CO_2 absorbed by the sea has been estimated at 53 gC m^{-2} yr^{-1}. Of this amount, about half was attributed to the flux caused by heat loss and the other half to biological production (Anderson et al., 2000). Higher estimates of annual fluxes, ranging from 40 to 85 gC m^{-2} yr^{-1}, were presented by Skjelvan et al. (2005 and reference therein). Total carbon in surface waters varies seasonally because of physical and biological processes that influence the amount of carbon exported to deep waters (von Bodungen et al., 1995; Noji et al., 1999). The mixing of the open ocean contributes to the transport of carbon from the surface to the deep interior. As a result of the increasing CO_2 input from the atmosphere, the pH in the Nordic Seas has decreased by ~0.0028 units per year in the period 1981-2019 (Frasner et al., 2022).

Here, we present data and main results obtained in the framework of the CASSANDRA (*advanCing knowledge on the present Arctic Ocean by chemical-phySical, biogeochemical and biological obServAtioNs to preDict the futuRe ChAnges*) project, funded by the Italian Arctic Research Programme (*https://www.programmaricercaartico.it/*). CASSANDRA contributed to the Synoptic Arctic Survey (SAS) by investigating the historical zonal transect at 75°N through the Greenland Sea Gyre during the summer of 2021 (29 August - 14 September). The SAS initiative aims to quantify the current state of the Arctic Ocean and its changes, focusing on water masses, ecosystems, and the carbon cycle (see https://synopticarcticsurvey.w.uib.no/). SAS sees the participation of 11 countries in 25 Arctic cruises.

2 DATA and METHODS

The LB21 CASSANDRA cruise (hereinafter, LB21 cruise) was carried out between 29 August 2021 (Longyearbyen, Svalbard) and 14 September 2021 (Bergen, Norway) on board the icebreaker Laura Bassi (https://www.ogs.it/en/research-vessel-laura-bassi). All methods used for the CASSANDRA activities were in line with the recommendations of the SAS and Go-Ship programme (https://www.go-ship.org/), the latter including the 75°N transect. This approach was chosen to obtain data that were as comparable as possible to other the SAS programme cruises. During the LB21 cruise, a total of 28 vertical Conductivity-Temperature-Depth (CTD) profiles were conducted at 20 hydrological stations (some stations include repeated casts). Of these, biogeochemical and biological data were also collected at 12 and 6 stations, respectively (see Fig. 1). Unfortunately, some technical problems and 2 days of adverse meteorological conditions in the middle of the cruise prevented the completion of all planned stations. Some of the figures presented here were created with Ocean Data View (Schlitzer, 2024).

2.1 Hydrographic data

All hydrographic profiles were recorded with a Seabird SBE911plus, equipped with some additional sensors. CTD measurements provide vertical profiles of *in situ* temperature (T) and conductivity (C) approaching the seafloor to ~ 5–10 m, depending on sea conditions. Potential temperature (θ),

salinity (S), and potential density anomaly (σ_θ, referred to 0 dbar) were calculated from *in situ* data using the MATLAB toolbox TEOS-10 (Gibbs SeaWater Oceanographic Toolbox) including the thermodynamic equations for seawater (http://www.teos-10.org/software.htm). Dissolved Oxygen concentration was measured using an SBE43 sensor. T and S data were quality checked and averaged every 1 dbar, with overall accuracy within $\pm$ 0.002 °C for T, $\pm$ 0.005 for S and 2% of saturation for oxygen. Fluorescence and turbidity in the water column were measured with optical sensors WET Labs ECO-AFL/FL. Water sampling was carried out using a rosette system equipped with 24 10-liter Niskin bottles.

2.2 Biogeochemistry data

The chemistry of seawater was investigated at 12 stations from discrete water samples (Fig. 1) by measuring dissolved oxygen, nutrients (nitrite, nitrate, phosphate, silicate), dissolved and particulate Carbon (DOC and POC), total dissolved nitrogen and phosphorus (TDN and TDP), $\delta^{18}O$ and δD of H_2O, inorganic carbonate system characterization by total alkalinity, pH_T and derived parameters. The dissolved oxygen concentration (DO) was determined by a potentiometric Winkler titration (Oudot et al., 1988; Grasshoff et al., 1999). Samples for inorganic nutrients (nitrite - NO_2, nitrate - NO_3, ammonium - NH_4, phosphate - PO_4 and silicate - $Si(OH)_4$) were collected and analysed as described in Ingrosso et al. (2016a) using a four-channel Continuous Flow Analyzer QuAAtro (Seal Analytical Inc., Mequon, WI, USA) autoanalyzer. Detection limits were 0.01 µmol L^{-1}, 0.02 µmol L^{-1}, 0.03 µmol L^{-1}, 0.01 µmol L^{-1} and 0.01 µmol L^{-1} for NO_2, NO_3, NH_4, PO_4 and $Si(OH)_4$, respectively. DON and DOP were calculated as the difference between dissolved total phosphorus (TDP) and PO_4 and between dissolved total nitrogen (TDN) and dissolved inorganic nitrogen (DIN $= NO_3 + NO_2 + NH_4$), respectively. TDP and TDN were determined as PO_4 and NO_3, respectively, after quantitative conversion to inorganic P and N by persulfate oxidation (Hansen and Koroleff, 1999). The accuracy and precision of the analytical procedures are annually checked through the quality assurance program (AQ1) QUASIMEME Laboratory Performance Studies (Wageningen, The Netherlands) and internal quality control samples were used during each analysis. Samples for pH_T analysis were collected and analysed on board as described in Ingrosso et al. (2016b) and Urbini et al. (2020) using a spectrophotometer (Varian Cary 50 UV-visible). The results were expressed on the 'pH total hydrogen ion scale' (pH_T) at 25°C, with a reproducibility of 0.0048, determined by replicates from the same Niskin bottles. To measure total alkalinity (A_T, µmol $kgSW^{-1}$), water samples were collected and analysed as described in Ingrosso et al. (2016a) and Urbini et al. (2020) using the seawater certified reference materials (CRMs) for TCO_2 and A_T supplied by Prof. A.G. Dickson, Scripps Institute of Oceanography, USA (Batch number #185) to calibrate HCl for analyses. A_T precision and the accuracy were less than $\pm$ 2.0 µmol kg^{-1}, assessed by analysing CRMs. All other carbonate system parameters, including pH_T at *in situ* temperature, seawater partial pressure of CO_2 (pCO_2), TCO_2, and aragonite saturation state (Ω_{ar}) were calculated using the CO2Sys program as described in Urbini et al. (2020). The estimated uncertainties were: $\pm$0.005 for pH_T at *in situ* temperature, $\pm$7.8 µatm for pCO_2, $\pm$5.6 µmol kg^{-1} for TCO_2 and $\pm$0.12 for aragonite saturation state. Samples for stable isotopic composition of dissolved inorganic carbon ($\delta^{13}C$-DIC) were collected in 12-mL Exetainer® (Labco Limited, Ceredigion, UK) evacuated glass tubes, containing 2 µL of saturated $HgCl_2$. Samples were stored at 4 °C in the dark until analysis was performed as described in Relitti et al. (2020). To determine the optimal extraction procedure for

209 water samples, two standard Na_2CO_3 solutions were prepared with a known ^{13}C value of $-10.8 \pm$
210 0.1 ‰ (k=1) and -4.2 ± 0.1 ‰ (k=1), respectively. The stable isotopic composition of dissolved
211 inorganic carbon is given conventionally in δ-notation in per mil deviation (‰) from the Vienna
212 Peed Dee belemnite (VPDB) standard.

213 For POC concentrations filters were freeze-dried and subsampled by punching 18% of the 45 mm
214 filter area and fitted into silver capsules/boats. The subsamples were treated with 1M HCl to remove
215 inorganic carbon and then placed into an oven at 60 °C until dry. Afterwards, the samples were
216 wrapped in tin capsules/boats to aid combustion during analysis. The samples were analyzed with
217 a Thermo Fisher elemental analyzer (FLASH 2000 CHNS = O) coupled with a Thermo Finnigan
218 DeltaC isotope ratio mass spectrometer (IRMS). At least two replicates were analysed for each
219 sample. Spatial variability was within ±2.5 % on the filter.

220 Water samples for DOC analyses were filtered aboard, immediately after collection, through
221 precombusted (4 h at 480 °C) Whatman GF/F glass fibre filters (0.7 µm nominal pore size).
222 Filtration was performed by using a disposable polycarbonate syringe and a polypropylene 25 mm
223 filter holder (Nuclepore), to prevent atmospheric contamination. Filtered samples were stored in 25
224 mL high density polyethylene (HDPE) bottles (previously treated with HNO_3 1.2 M at 50 °C for 1
225 h) which were quickly frozen in an aluminium block at -20 °C. In the laboratory, filtered samples
226 were thawed, acidified to pH = 2 with ultrapure HCl and purged with N_2 for about 10 min to remove
227 inorganic carbon, as outlined in Pettine et al. (2001). Dissolved organic carbon (DOC) was assayed
228 by high temperature catalytic oxidation (HTCO) using a Shimadzu TOC-L series analyser.

229 Samples for stable isotope ratio measurements in seawater were collected in 5 mL amber glass
230 bottles. The bottles were filled to avoid the presence of air, immediately sealed and stored at a
231 temperature of 4 °C until the analyses. Analyses were performed by means of a Thermo DeltaV-
232 Advantage mass spectrometer equipped with a gas-bench. For the analysis, a quantity of 200 μL of
233 water sample was used in a glass vial firmly closed with a membrane cap. The samples were flushed
234 with a gas mixture of 2% H in helium with a purity of 99.998 and analysed to determine δD.
235 Immediately after the δD analyses, the same samples were flushed with a gas mixture of 0.4% CO_2
236 in helium with a purity of 99.998 and analysed to determine $\delta^{18}O$ after 20 hours of equilibration.
237 All samples were measured at least in triplicate and the isotopic data are the mean of consistent
238 results. The standard deviation of our results is always 0.50‰ and 0.06‰ or better for δD and $\delta^{18}O$,
239 respectively. The SMOW2 and SLAP2 isotopic standards were used as a reference together with a
240 'home-made' standard. The home-made standard is analysed every 3 measurements (3 replicates of
241 a single sample) to assess the stability of the measurements. The isotopic composition is expressed
242 as:

243 $$\delta X = [(R_s - R_r)/R_r] \times 1000$$

244 where δX represents δD or $\delta^{18}O$, R=D/H or $^{18}O/^{16}O$ in the sample (s) and in the reference (r),
245 respectively.

2.3 Phytoplankton data

2.3.1 Total and size-fractionated chlorophyll *a* (chl-*a*)

Chlorophyll *a* (chl-*a*) and phaeopigment (phaeo) concentration were measured fluorometrically. Samples were filtered on Whatman GF/F glass-fiber and polycarbonate membranes (of 2.0 and 10.0 µm) to separate three size fractions: micro-phytoplankton (> 10 µm), nano-phytoplankton (10–2.0 µm) and pico-phytoplankton (2.0–0.45 µm) as reported in Decembrini et al. (2021).

2.3.2 Utermöhl phytoplankton

For the determination of Utermöhl phytoplankton (i.e., all species/taxa detectable by light microscopy, thus excluding prokaryotic phytoplankton and the majority of picoeukaryotes < 1 µm), 500-mL water samples were collected in opaque polyethylene bottles and immediately fixed with pre-filtered and neutralised formaldehyde (1.6% final concentration) (Throndsen, 1978). Inverted microscopes equipped with phase contrast (Zeiss Axiovert 200M and Leica DMi8) were used for the taxonomic identification analysing a variable volume of sample (10-50 mL), according to the Utermöhl method (Zingone et al., 2010). Counting was performed along transects across the microscope chambers at a magnification of 400x for small (5-20 µm) or very abundant species and observing half of the sedimentation chamber at a magnification of 200x for less abundant microphytoplankton (> 20 µm). The abundance was expressed as the number of cells per liter (cells L^{-1}). The minimum value of the counted cells was 200 cells per sample for a confidence limit of 14% (Andersen & Throndsen, 2004).

2.4 Zooplankton data

2.4.1 Microzooplankton

Microzooplankton (MZP) samples were collected in six stations at different depths depending on water column vertical profiles (Fig. 1). For MZP analyses, 10 L of seawater were reverse filtered through a 10 µm mesh to reduce the volume to 250 mL and immediately fixed with buffered formaldehyde (1.6% final concentration). Subsamples (50 mL) were then examined in a settling chamber using an inverted microscope (magnification 200x) (Leitz Labovert, Leica DMI 300B), following the Utermöhl method (1958). The entire surface of the chamber was examined. Among the MZP community, five main groups were considered: heterotrophic dinoflagellates, aloricate ciliates, tintinnids, micrometazoans and other rare protozoans. Tintinnids empty loricae were not differentiated from filled loricae because the tintinnid protoplasts are attached to the lorica by fragile strands that can easily detach during the collection and fixing of the samples. For each taxon, the biomass was estimated by measuring the linear dimensions of each organism with an eyepiece scale and relating the shapes to standard geometric figures. Cell volumes were converted into carbon values using the appropriate conversion factors, as follows: aloricate ciliates, pg C $cell^{-1}$ as μm^3 x 0.14 (Putt and Stoecker, 1989); tintinnids, pg C $cell^{-1}$ as μm^3 x 0.053 + 444.5 (Verity and Langdon, 1984); athecate heterotrophic dinoflagellates, pg C $cell^{-1}$ as μm^3 x 0.11 (Edler, 1979); thecate heterotrophic dinoflagellates, pg C $cell^{-1}$ as μm^3 x 0.13 (Edler, 1979); other protozoans, pg C $cell^{-1}$ as μm^3 x 0.08 (Beers and Stewart, 1970).

2.4.2 Mesozooplankton

Three hauls were conducted at six stations (Fig. 1): one horizontally at the surface with the Manta net (333 µm, 0.098 m^2 net opening) and 2 vertically (from 100 m depth to the surface) with the WP2 net. A Hydrobios flowmeter mounted in the net opening was used to measure the volume of seawater filtered through each net. Immediately after the catch, samples were treated to estimate biomass, taxa composition and abundance of the zooplanktonic community. Samples collected with the Manta net were split by using the Huntsman beaker technique (van Guelpen et al., 1982) and treated as follows: half of the sample was fractionated by passing it through a series of steel sieves with decreasing mesh size (> 2 mm; 2-1 mm; 1-0.5 mm; 0.5-0.2 mm) and immediately frozen at -20°C for biomass analysis, ¼ was fixed and preserved in a seawater-buffered formaldehyde solution (4% final concentration) for later determination of taxa composition and abundance and ¼ was fixed in 96% ethanol for molecular analysis (data not shown in this manuscript). Samples collected with the WP2 net were treated as follows: one sample was entirely fractionated and frozen at -20 °C for biomass analysis using the same procedure as the Manta net samples, and one sample was split in half and fixed in seawater-buffered formaldehyde solution (4% final concentration) and 96% ethanol, respectively. In the laboratory, to estimate biomass (dry mass), each size fraction was resuspended in a small volume of filtered seawater and dewatered by vacuum filtration on pre-dried and weighed GF/C filters (47 mm diameter) after being briefly rinsed with distilled water to remove the salts of the seawater (Postel et al., 2000). Each filter was then placed in a small plastic Petri dish and dried in an oven at 60 °C for 24 hours or longer until completely dry and weighed on an electronic microbalance. The fixed samples were concentrated to remove the formaldehyde, and the organisms were suspended in filtered seawater and carefully passed through the same set of sieves used for the biomass. Depending on the abundance, the organisms present in the subsamples or in the entire fractionated sample were counted and identified (Copepoda, Chetognata, Mollusca, and others) under stereo-microscopes (Leica 165C :120x; Leica 205C: 160x).

2.5 Microbiological data

2.5.1 Prokaryotic biomass, viable and dead cells, respiring cells

The microbial components were investigated by using different approaches. The detailed methodological procedures for assessing prokaryotic cell abundances, biomass and morphometric features are reported by La Ferla et al. (2012). The viability of prokaryotic cells quantified by the Live/Dead Bac Light Bacterial Viability Kit™ and the number of respiring cells quantified by the Bac Light Redox Sensor CTC Vitality Kit™ were estimated as reported by Azzaro et al. (2022).

2.5.2 Physiological profiles of microbial community

Physiological profiles were determined by the Biolog EcoPlate™ microplate assay. The metabolic potentials of bacterial assemblages were quantified as the optical density (OD) values of the formazan produced by oxidation of the 31 carbon sources included in the Biolog Ecoplates. The absorbance was recorded at 590 nm excitation wavelengths using a compact plate reader Byonoy Absorbance 9 and spectrophotometrically measured according to Azzaro et al. (2022) and references therein.

2.5.3 Microbial activities involved in organic matter decomposition and mineralization (enzymatic and respiratory activity rates)

The potential decomposition rates of organic polymers (proteins, polysaccharides and organic phosphates), mediated by the microbial enzymes leucine aminopeptidase (LAP), beta glucosidase (GLU) and alkaline phosphatase (AP) respectively, were estimated by incubation with fluorogenic substrates derived from methylcoumarin (MCA) and methylumbelliferone (MUF), as reported by Hoppe (1993), adapted by Caruso et al. (2020). Fluorescence readings were converted into enzymatic activity rates and expressed as the maximum rate (Vmax) of hydrolysis of the substrates, in nM h^{-1}.

2.5.4 Respiratory activity

The respiration rates were measured by the Electron Transport System activity (ETS) assay. This method is based on the conversion of tetrazolium salt into formazan. The detailed methodological procedures were reported by Azzaro et al. (2006, 2021) and references therein.

3   RESULTS

The LB21 cruise (see Fig. 1) was conducted in early September, when the seasonal minimum of sea ice extent is recorded in the Arctic and sub-Arctic regions (Fig. 2). The ice extent in the Fram Strait fluctuates from year to year. In the long term, the lowest extent in September was recorded exactly in 2021, the highest in 1987. After 2021, a slight recovery of the summer seasonal sea ice extent was observed. For winter, the lowest extent was observed in 2006, the highest in 1986. Our cruise therefore took place during the period of the lowest summer sea ice extent measured to date.

343
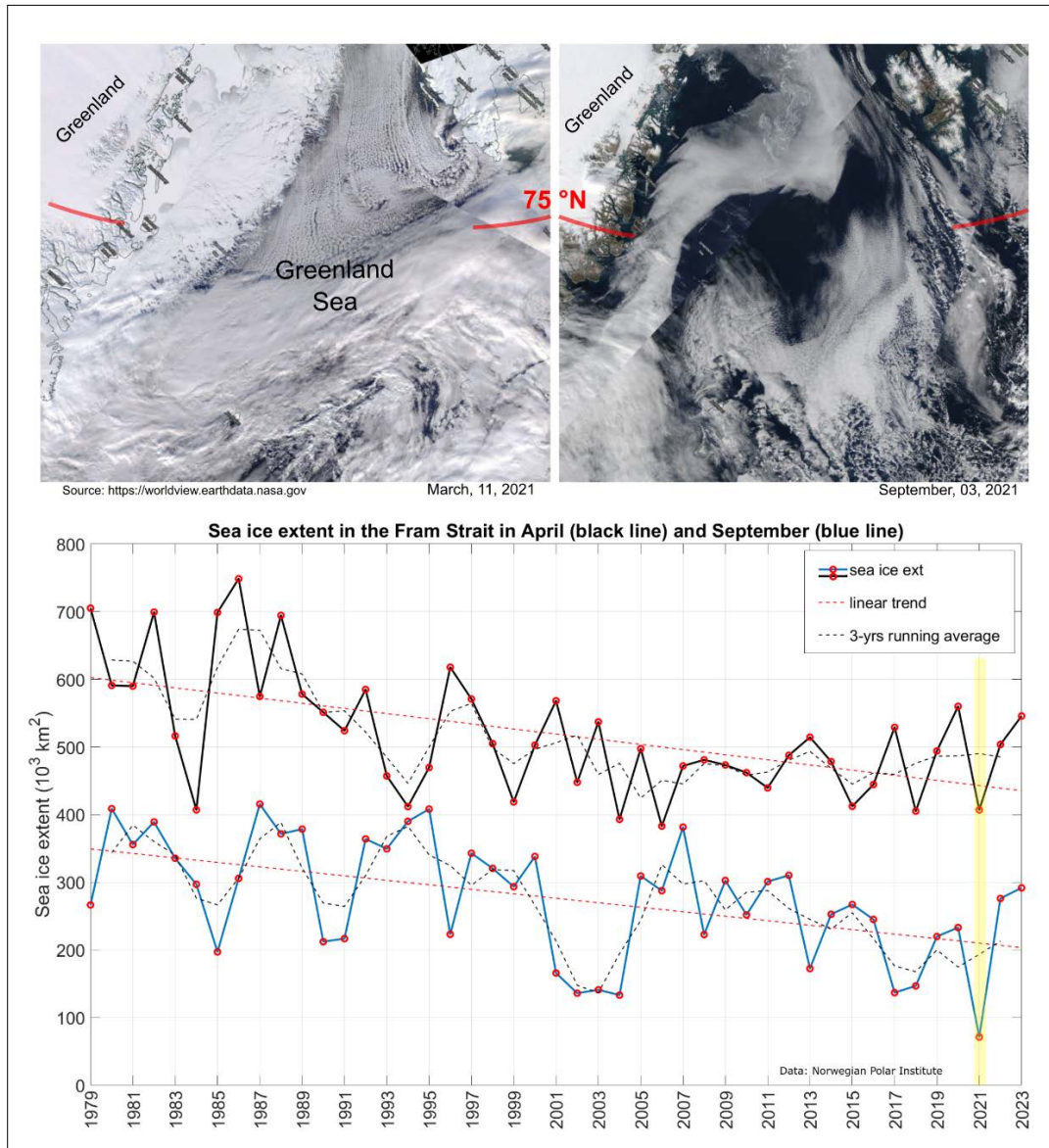
Figure 2 - **Upper panels**: satellite images of the Greenland Sea and the Fram Strait in March and September 2021
(MODIS Corrected Reflectance Imagery, source NASA). **Bottom panel**: April (black line) and September (blue line)
mark the annual maximum and minimum sea ice extension in the Fram Strait (source: Norwegian Polar Institute, 2024,
Environmental monitoring of Svalbard and Jan Mayen (MOSJ). URL: https://mosj.no/en/indikator/climate/ocean/sea-
ice-extent-in-the-barents-sea-and-fram-strait/). The yellow vertical bar indicates the year 2021.

3.1 Physical Oceanography: thermohaline properties distribution

We grouped our data according to the definition of main water masses from Rudels et al. (1999)
and Wang et al. (2021) and adjusted them to include most of our data. Due to some data gaps, it
was not possible to define all relevant water masses in this area more precisely. Along the zonal
transect at 75 °N, the ocean temperature shows a very pronounced horizontal gradient, with typical
values of AW (θ > 3.0 °C, S > 35) in the uppermost 500 m of the water column on the eastern side
(Fig. 3). At the surface, the AW has temperatures between 4.5 °C and 9.0 °C (Fig. 4). The AW
extends to the west and gradually becomes shallower, so that from station 20 to station 35 it only
occupies the uppermost 50-80 metres. In contrast, the surface layer on the western side, from station
38 to 46, has a thin (about 40-80 m) layer of Polar Water (PW) with temperature and salinity values

359   that are typical of sea ice meltwater ($\theta < 0$ °C, S $\leqq$ 33). The intermediate zone between 100 m and
360   500 m is largely occupied by mixed water and we refer to it as the transition layer. The deep layer
361   below 500 m depth is occupied by Greenland Sea Arctic Intermediate Water (GSAIW, $-0.9 < \theta < 0$
362   °C, S $\sim$ 34.9), Greenland Sea Deep Water (GSDW, $\theta < -1.0$ °C, S < 34.9) in the central and
363   westernmost part, respectively, and Norwegian Sea Deep Water (NSDW, $\theta \sim -1.0$ °C, S $\sim$ 34.9) in
364   the easternmost part of the section. We find that the deep layer below 500 m has homogeneous
365   thermohaline properties, with a slightly pronounced difference at the easternmost edge where the
366   NSDW flows northwards. Isotherm at 0 °C and the overall distribution of isopycnals (Fig. 3 a, c)
367   show a classic dome shape with an upwelling in the central part caused by the effect of the GSG,
368   which tends to lift the intermediate water towards the surface due to its cyclonic (i.e., anticlockwise)
369   sense of rotation. In addition, we are certain that the strong horizontal shear and local meteorological
370   conditions can induce the formation of several mesoscale structures (i.e., eddies, hardly shown by
371   our spatial resolution ranging from about 20 km (along the sides) to 40-60 km (in the centre of the
372   transect). They can change the internal distribution and even trap nutrients and other chemical-
373   biological properties. The dissolved oxygen values show a higher oxygen enrichment (> 350 µmol
374   kg^{-1}) in the intermediate layer between stations 15 and 38 (Fig. 3d), while the maximum values are
375   found in the upper layer near the Greenland coasts, where the PW flows southwards. In contrast,
376   lower oxygen values (< 300 µmol kg^{-1}) are found below 1500 m depth and in the easternmost part
377   of the section where AW and NSDW occur (Fig. 3d). Turbidity is higher at the surface and along
378   the continental slopes, both on the eastern and western sides, while the fluorescence maximum is at
379   a depth of about 25-30 m and higher values are found in the easternmost part of the section (Fig.
380   3e, f). Overall, θ spans from 1.5 °C to almost 9.0 °C, while S spans from 30 (melting waters) to 35
381   (AW, Fig. 4).
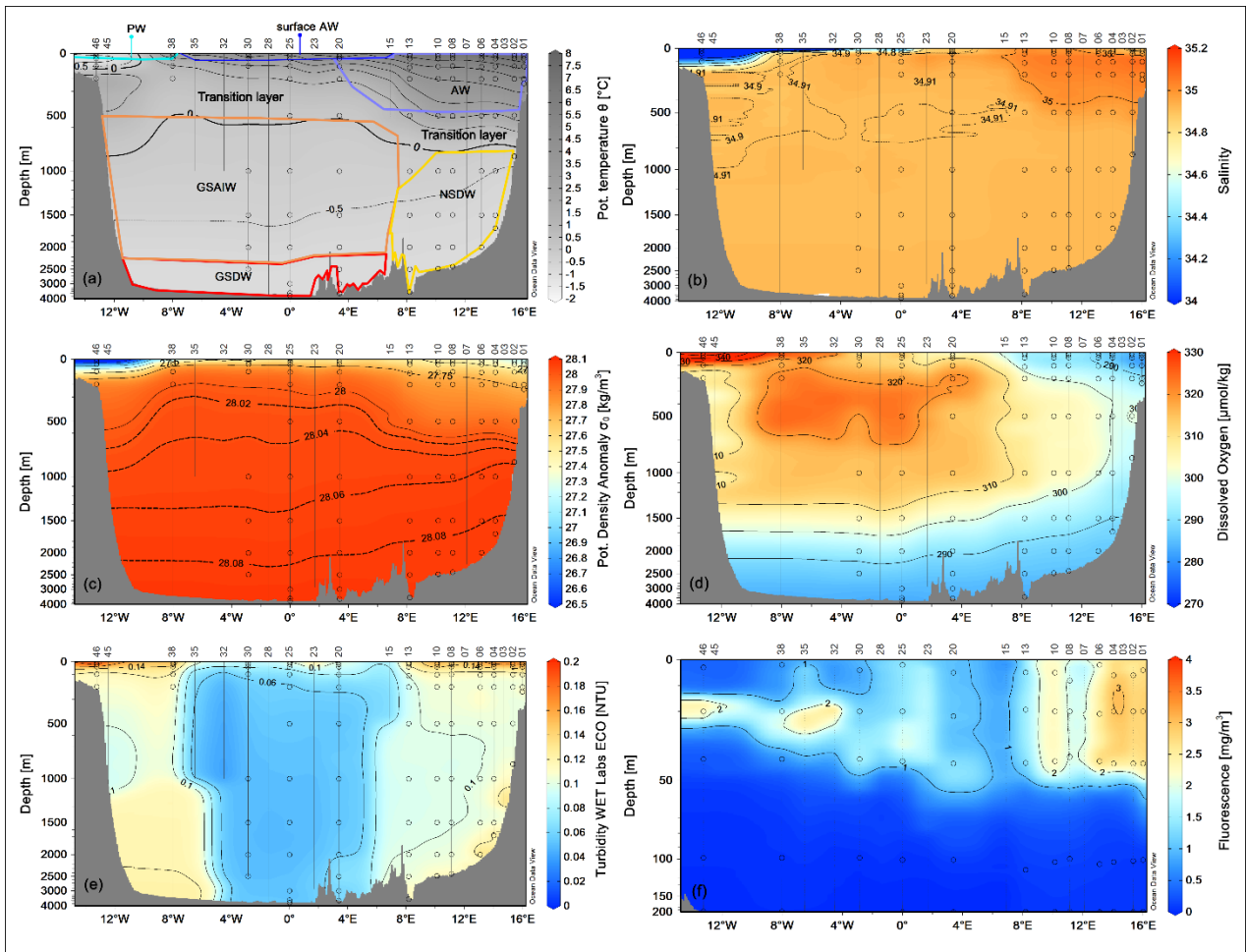
Figure 3 - Vertical distribution of (a) potential temperature (°C), (b) salinity, (c) potential density anomaly (kg m^{-3}), (d) dissolved oxygen (µmol kg^{-1}), (e) turbidity (NTU), and fluorescence (mg m^{-3}) along the zonal transect at 75° N in September 2021. The empty dots indicate the sampling points of the Niskin bottles. Panel a show also the distribution of principal water masses according to their core values [**AW** - Atlantic Water; **GSAIW** - Greenland Sea Arctic Intermediate water; **NSDW** - Norwegian Sea Deep Water; **GSDW** - Greenland Sea Deep Water; **PW** - Polar Water or Melting Water]. Depths on y-axis are non-linear.
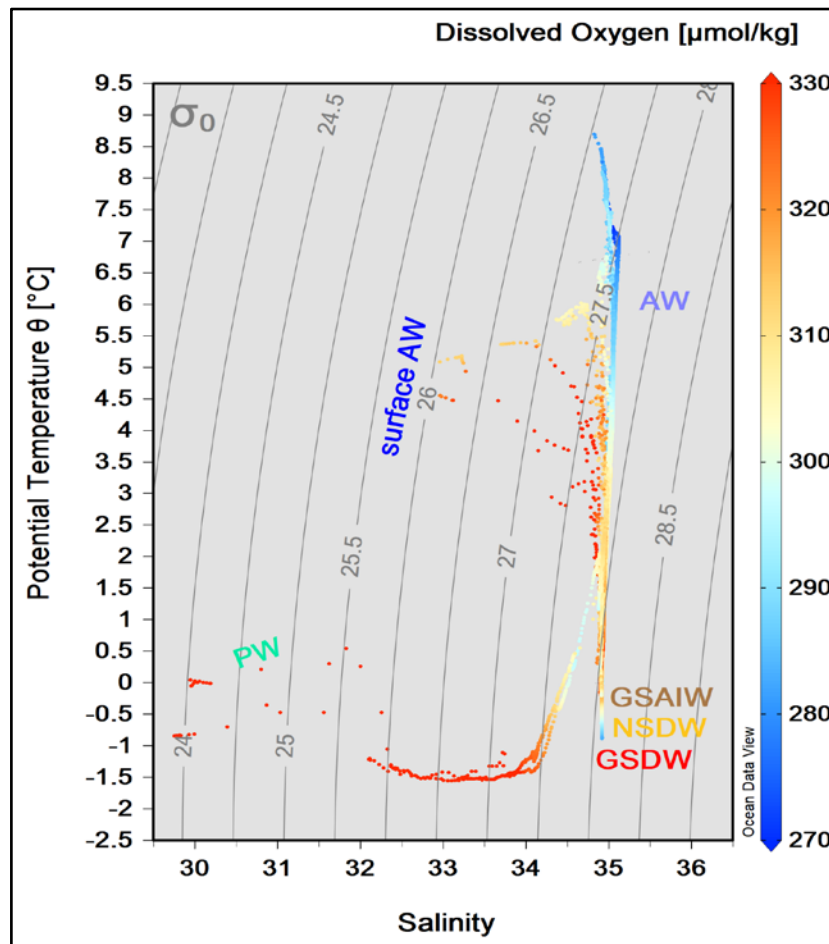
Figure 4 - θ/S diagram from the CTD data collected along the 75 °N section, during the LB21 cruise in September 2021. The colorbar on the right-hand side refers to the values for dissolved oxygen concentration (µmol kg⁻¹). [For water masses acronyms see caption of figure 3].

3.2 Biogeochemistry

Along the entire transect, except for the two edges, the seasonal warming in summer had created a well-stratified upper layer about 30-50 metres deep. At the surface, the central Greenland Sea appears to be almost nutrient poor (Fig. 5). The western side of the transect is characterised by higher concentrations of phosphate and silicate, good indicators of the upper halocline of Arctic surface water along the Greenland slope, whereas nitrate concentrations are very low. At depth, NSDW and GSDW (see Fig. 3, 5) were enriched with silicate.

402
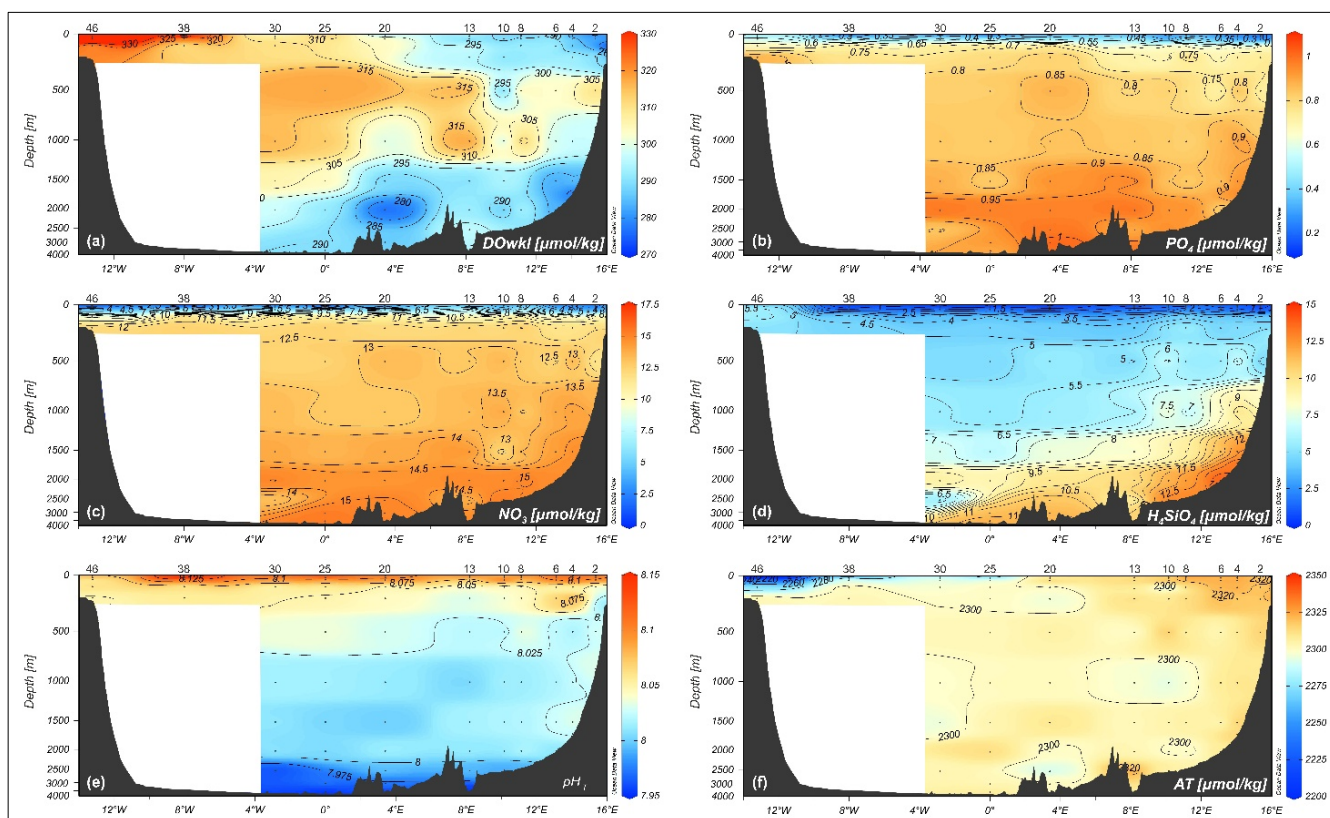
Figure 5 - Vertical distribution of (a) dissolved oxygen concentration (μmol/kg), (b, c, d) nutrients concentration (μmol/kg), (e) pH_T, and (f) Total Alkalinity (μmol/kg) along the zonal transect at 75° N during the LB21 cruise in September 2021. Data are obtained from the laboratory analyses on water samples. Depths on y-axis are non-linear.

A marked vertical gradient is found along the entire transect with higher pH_T values (up to 8.227, Fig. 5e) in the photic layer (< 100 m depth) decreasing with increasing depth and reaching the lowest values (7.946-7.997) in the deep layer of the Greenland Sea, presumably due to the degradation of settling organic matter. High total alkalinity values (Fig. 5f) are found on the easternmost side where the AW and NSDW flow northwards. The highest values (A_T up to 2320-2348 μmol kg^{-1}) are found in the higher salinity AW and particularly in the photic layer also due to the contribution of photosynthetic activity. The lowest values are instead associated with fresh Polar Water found at the surface on the westernmost part of the section.

At the surface layer, a high variability in the organic matter pool (POC and DOC) is observed (Fig. 6); a decreasing trend down to 1000 m depth and an increase towards greater depths characterise the vertical profiles of DOC. POC concentrations range from 11.2 μg C L^{-1} (St 30, at 2002 m depth; 0.93 μM C) to 160 μg C L^{-1} (St 46, at 198 m depth; 13.3 μM C). A greater variability with depth is observed (coefficient of variation higher than 65). The highest values are generally found at the surface and within the depth interval of 20–40 m. The highest (mean) concentration is measured at station 46 (80.5 ± 53.4 μg C L^{-1}), while slightly lower (mean) values are found at stations 1, 30 and 38 (67.2 ± 46.8; 41.0 ± 23.1 and 60.0 ± 15.3 μg C L^{-1}, respectively), and the lowest values are found at stations 10 and 20 (34.1 ± 31.0 and 28.2 ± 20.5 μg C L^{-1}, respectively). DOC shows classic vertical profiles, with the highest concentrations (1.22 mg C L^{-1}; 101.7 μM C) at station 30 (20 m depth) and a decrease to a minimum of 0.5 mg C L^{-1} (41.7 μM C) at station 10 (499 m depth). Between 200 and 1000 m depth, the values remain low (mean 0.83 ± 0.22 mg C L^{-1}; 69.2 ± 18.3

428   µM C), while a slight increase was observed in the bottom water, particularly at stations 20 and 10
429   (Fig. 6).

430
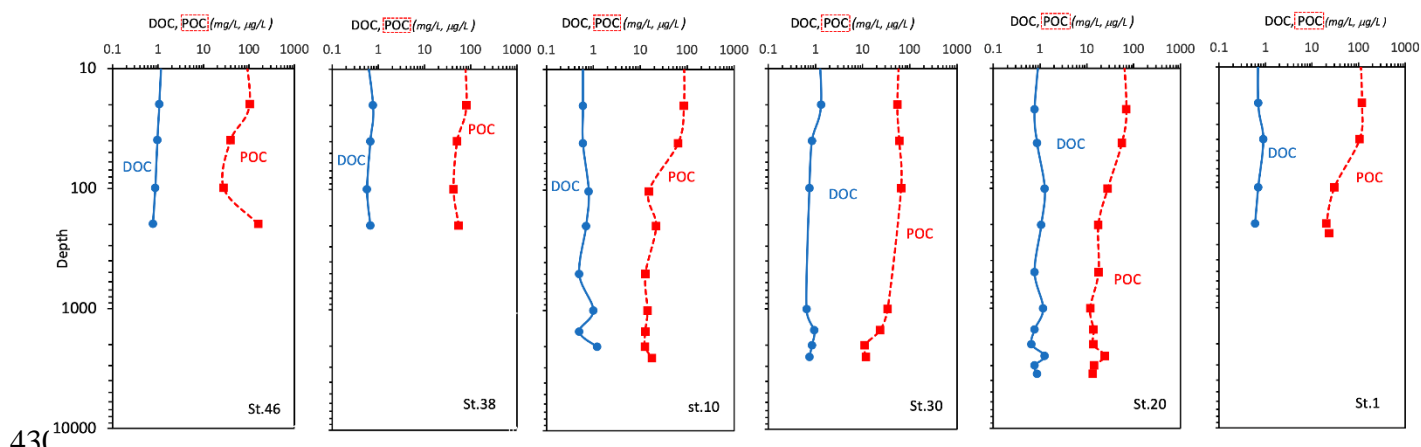
431   **Figure 6 -** Vertical profiles of Dissolved Organic Carbon (DOC, mg L⁻¹) and Particulate Organic Carbon (POC, µg L⁻
432   ¹) concentrations; Data are represented in natural log (*ln*) scale.

433   The isotope values in the total of 96 analysed samples range from -0.43 to 0.8‰ for $\delta^{18}O$ and from
434   -2.51 to 5.36‰ for δD. Along the transect, a gradient from west to east can be seen in the surface
435   waters, with lower values for $\delta^{18}O$ and δD on the westernmost side (Fig. 7). The lowest values at
436   the surface in the westernmost part of the section could be related to fresh PW, while the higher
437   values in the easternmost part could be related to northward flowing AW. At depths between 500
438   and 1000 m, isotope values drop to a relative minimum, while maxima occur near the bottom at
439   stations 20 and 25, where GSDW is identified. In addition, a minimum is observed at depth at
440   stations 8 and 10, in an area occupied by NSDW.

441
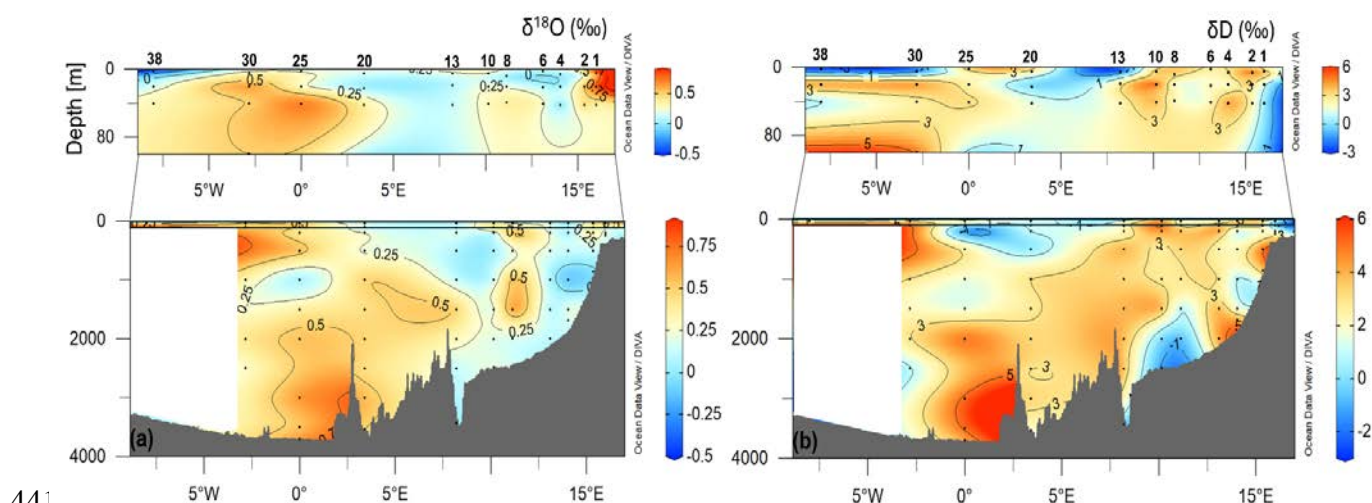
442   **Figure 7 -** Vertical distribution of $\delta^{18}O$ (a) and δD (b) along the zonal transect at 75° N during the LB21 cruise in
443   September 2021.

3.3 Phytoplankton

3.3.1 Total and size-fractionated chlorophyll *a* (chl-*a*)

Integrated total chl-*a* in the euphotic layer (0-100 m) averages 55.4 mg m^{-2}, while the highest concentrations (73.1 mg m^{-2}) are found at stations located at the ends of the transect (65.3 mg m^{-2}) close to the continental shelf (Fig. 8). The concentration of chl-*a* at different depths ranges between 0.20 mg m^{-3} (st.1, 100 m) and 2.90 mg m^{-3} (st. 1, 20 m) with an average value of 0.63 ± 0.64 mg m^{-3}. Degraded pigments (phaeo) are around 40% with respect to chl-*a*. The size spectrum of the phytoplankton community biomass along the water column, shows different percentage contributions to the total with 65% for the nano-phytoplankton, 21% for the micro-fraction and 14% for the pico-phytoplankton (Fig. 8). Exception to this composition is observed in the westernmost station (st. 46) where the micro-fraction dominates, replacing the nano-phytoplankton.
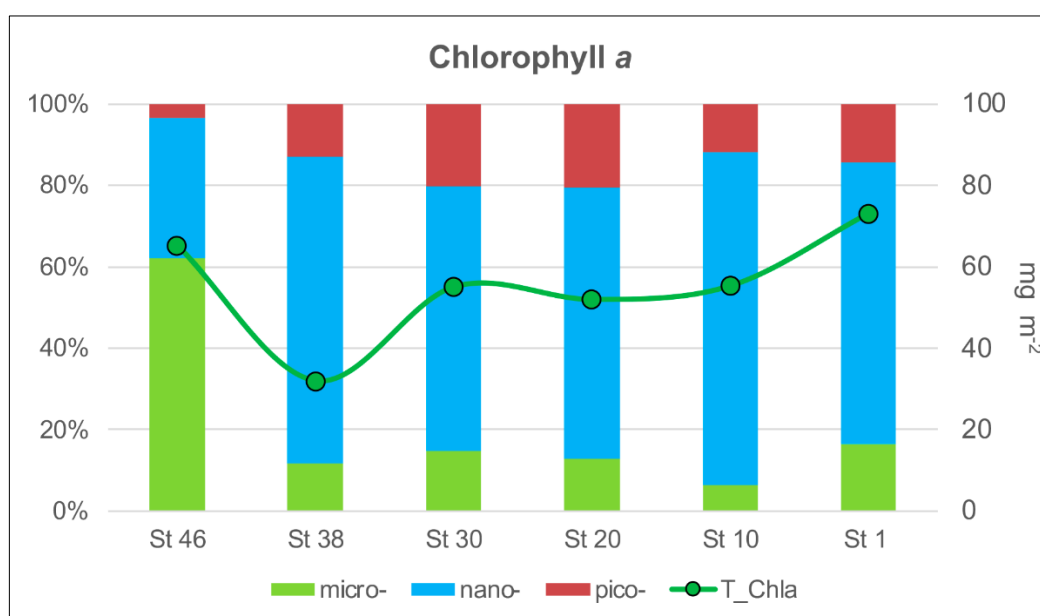
Figure 8 - Integrated total chl-*a* concentration (0-100 m depth) at the stations along the 75°N zonal transect (green line) with the percentage of contribution of micro- nano- and pico-phytoplankton size-fractions (histogram).

3.3.2 Phytoplankton composition and abundances

The phytoplankton analyses do not reveal a clear pattern along the transect, although some differences in abundance and composition were observed. The integrated abundances of phytoplankton, ranging from 7.00 (st. 30) to 23.48 x 10^4 cells L^{-1} (st. 20), are higher at the easternmost stations than at the westernmost ones (on average 19.33 x 10^4 cells L^{-1} at stations 1, 10, 20 and 9.44 x 10^4 cells L^{-1} at stations 30, 38, 46, see Fig. 9). This is mainly due to a more even vertical distribution of abundance at the eastern stations. In contrast, the westernmost stations have even higher phytoplankton abundances, but limited to subsurface maxima, like 50.40 x 10^4 cells L^{-1} at 38 m at station 20, while abundances in the rest of the water column are very low. The phytoplankton community along the transect is characterised by the dominance of the flagellate group (70% of the total phytoplankton), mainly represented by small (< 10 μm) forms with uncertain taxonomic identification (on average, 61%). Diatoms (on average, 9% of the total phytoplankton) are present in very low abundances in the easternmost and central stations (on average, 0.43 x 10^4 cells L^{-1} at stations 1, 10, 20, 30), while higher values were recorded in the two westernmost stations

473   38 and 46 (on average, 3.24 x 10^4 cells L^{-1}). Finally, dinoflagellates accounted for an average of

474   21% of the total phytoplankton, with higher abundances occurring in the easternmost stations than

475   in the westernmost stations (3.32 x 10^4 cells L^{-1} and 1.42 x 10^4 cells L^{-1}, respectively).

476
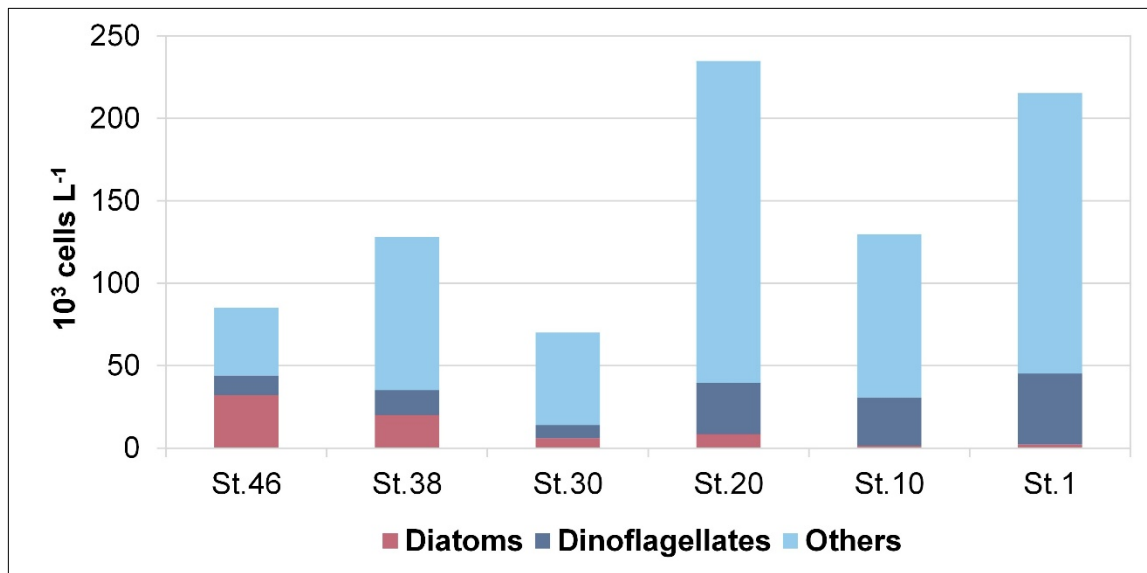
477   **Figure 9 -** Integrated values (0-100 m) of abundance (cell. L^{-1}) of the main phytoplankton groups (diatoms,
478   dinoflagellates and others) at the sampled stations along the 75°N transect.

3.4 Zooplankton

3.4.1 Microzooplankton abundance and biomass

481   The MZP abundance in the study area varies between 721.5 ind. L^{-1} (st. 38, at 0 m) and 6.25 ind. L^{-1}
482   ^{1} (st. 20, at 3500 m). The carbon content shows higher values at the surface with a maximum value

483   of 1.7 µgC L^{-1} (st. 38, 0 m) and a minimum of 0.01 µgC L^{-1} at 2520 m depth (st. 10). The vertical

484   distribution of organisms, based on their abundance along the water column, shows higher

485   abundances in the first 200 m, compared to the zone > 200 m. In particular, the integrated abundance

486   of MZP in the upper layer reaches its maximum at st. 38, mainly due to the higher presence of

487   tintinnids, while the lowest values are found at st. 20, in the centre of the transect (Fig. 10). The

488   highest carbon content is recorded at st. 10, which is due to the high abundance of other protists and

489   micrometazoans (Fig. 10). Tintinnids are the most abundant taxa in the study area, followed by

490   heterotrophic dinoflagellates and aloricate ciliates (Fig. 10).

491
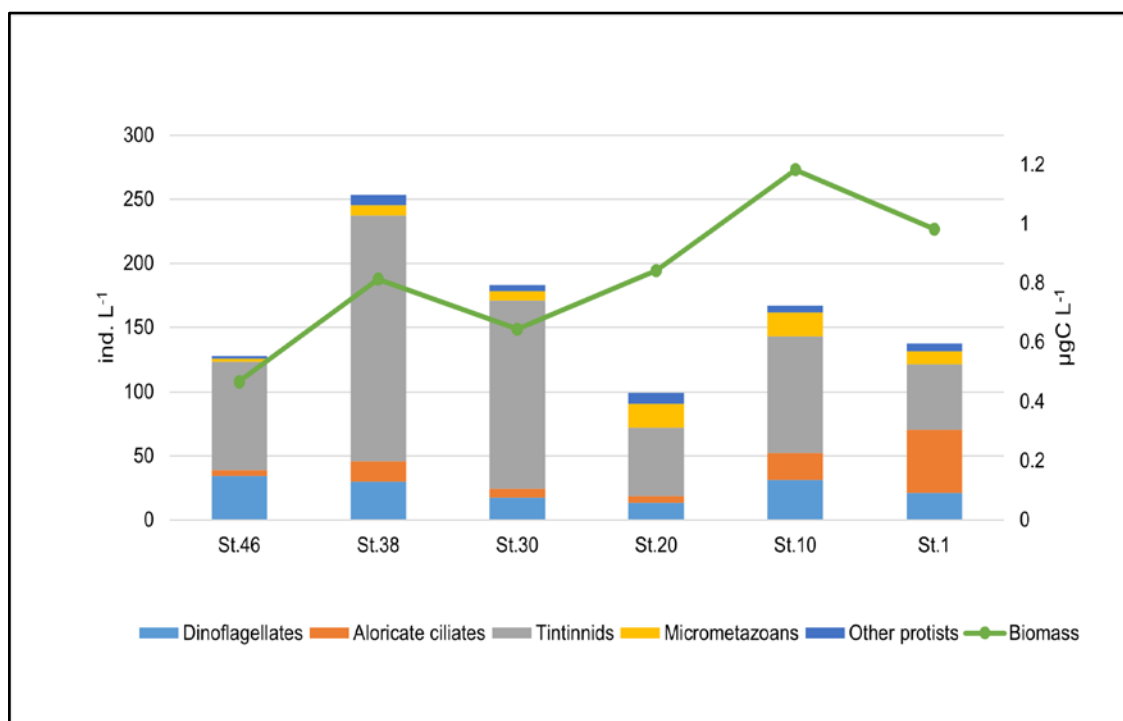
Figure 10 - Integrated values (0-200 m) of abundance (ind. L^{-1}) and biomass (µgC L^{-1}) of microzooplankton groups (dinoflagellates, aloricate ciliates, tintinnids, micrometazoans and other protists) at the sampled stations along the 75°N transect.

3.4.2 Mesozooplankton biomass and abundance

Biomass and abundance of mesozooplankton have the same distribution along the transect both at the surface (ca. 20 cm depth, Fig. 11a) and in the upper layer (0-100 m depth, Fig. 11b), with the highest values found in the central part of the transect (st. 20). Nevertheless, the surface samples are richer in organisms than those collected in the water column (mean abundance: Manta net: 1257 ± 1110 ind. m^{-3}; WP2 net: 492 ± 387 ind. m^{-3}), which also corresponds to a higher biomass (mean biomass: Manta net: 41 ± 32 mgDM m^{-3}; WP2 net: 10 ± 7 mgDM m^{-3}). Overall, organisms 1-2 mm in size account for 61 % of the mesozooplanktonic biomass in the surface waters and are the most abundant at almost all stations (Fig. 11a), while in the samples collected with the WP2 net, the biomass fractions consisting of organisms 1-2 mm and > 2 mm in size were the most abundant, accounting for 35 and 38 % of the total biomass, respectively (Fig. 11b). Copepods are the most abundant taxon both at the surface and in the upper layer (97 % and 94 % of the total mesozooplankton abundance, respectively), mainly represented by the genus *Calanus*. Chaetognaths, although much less abundant than copepods, are found along the entire transect both at the surface and in the upper layer, being most numerous at stations 10, 20, and 30. Molluscs are almost absent in the surface water and are mainly found in the water column at the eastern stations of the transect (st. 1 and st.10).

512
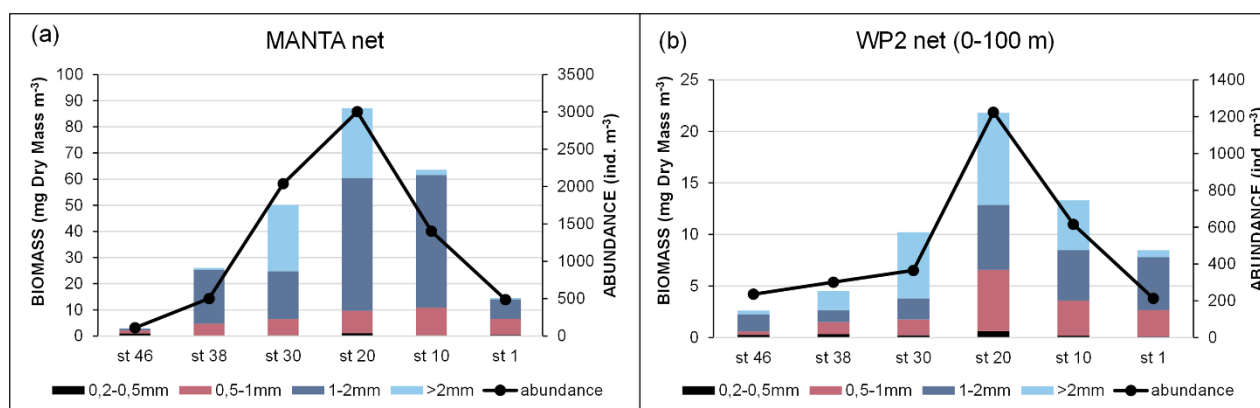
Figure 11 - Biomass and abundance of mesozooplankton: (a) Manta net sampling at surface and (b) WP2 net sampling
in the 0-100 m layer.

3.5 Microbial compartment: abundance, biomass, and activities

The abundance of prokaryotes is high in the photic (0-100 m depth) layer (range: 5.57 to 11.3 x
10^5 cells m^{-3}) and decreases with depth. The highest values are measured at stations 20 and 1. From
100 to 1000 m depth, the abundance ranges from 1.75 to 3.21 x 10^5 cells m^{-3} and from 0.53 to 0.64
x 10^5 cells m^{-3} at greater depths. The cell volume ranges from 0.049 to 0.098 µm^3, with a mean
value of 0.072 ± 0.018 µm^3. In the photic and aphotic layers, the cell volumes vary in a similar
range (0.08 ± 0.02 µm^3). The highest volumes at great depths characterise stations 30 and 10, where
large, curved rods are observed. Apart from stations 30 and 10, data show a similar vertical profile
in the size distribution. The highest percentage of live cells (about 33%) is observed at station 46
in the photic layer. However, peaks are also found in the deeper layers. The number of respiring
cells (CTC+) is in the order of 104 cells mL^{-1}. Variability between the layers is observed at all
stations. In general, the high proportion of respiring cells below 100 m depth is observed at stations
46, 30 and 20. Conversely, the higher percentages are found in the photic layer at stations st. 10
and 1 (Fig. 12).

529
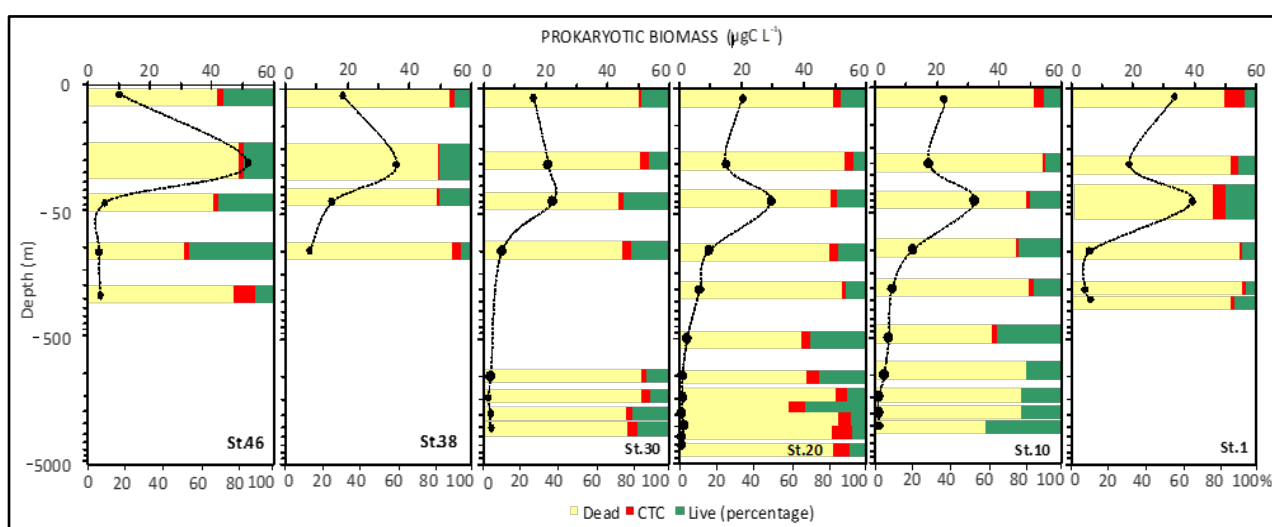
Figure 12 - Vertical profiles of prokaryotic biomass, viable and dead cells (Live/Dead) and respiring cells (CTC); Data
on y axis are represented in natural log (*ln*) scale.

Overall, the average percentages of carbon source utilisation determined by Biolog Ecoplates show
that carbohydrates and carboxylic acids were well-utilised polymers at each station and in each

layer. Especially in the aphotic layer, the percentage utilisation is highest at most stations. Complex carbon sources and phosphate carbon are utilised at similar percentages throughout the water column; conversely, amino acids are preferentially utilised in the aphotic layer. Amines are only little used (Fig. 13).
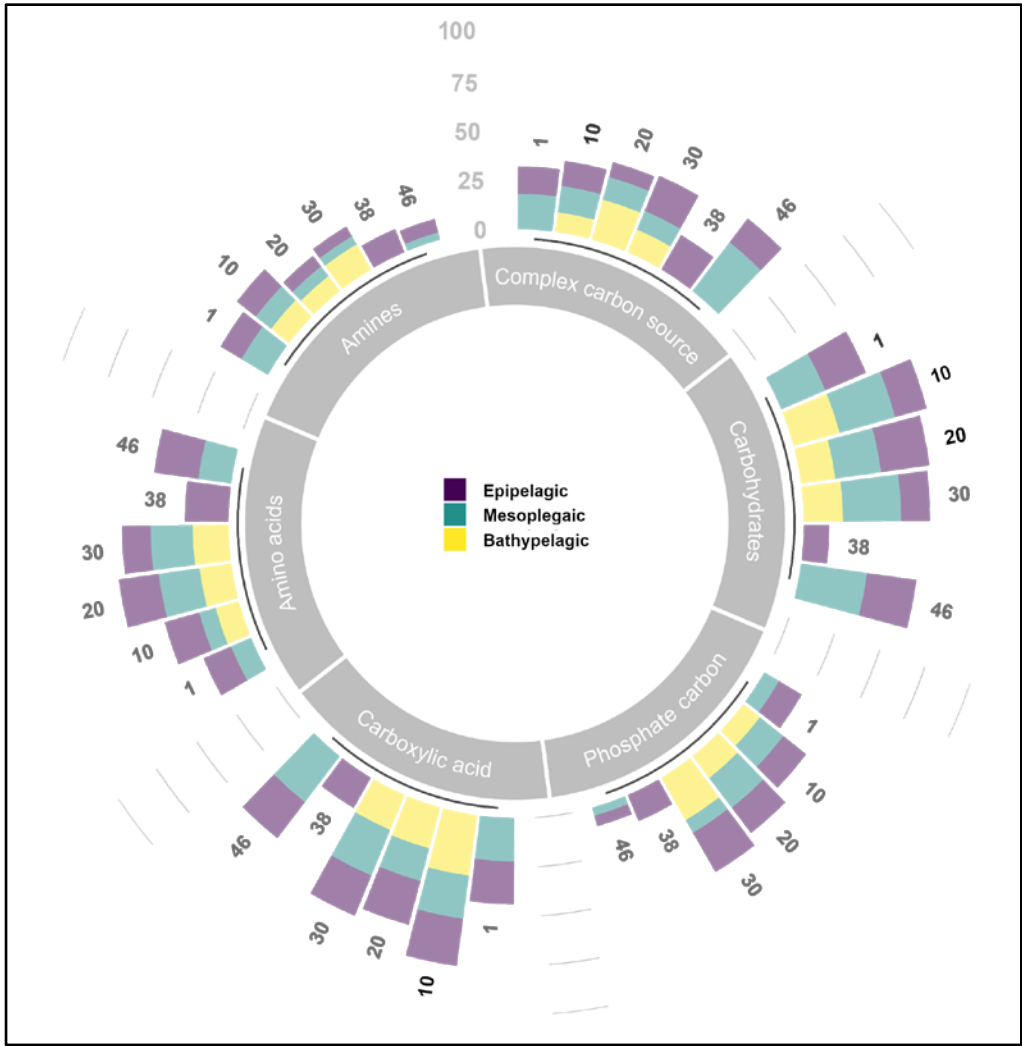
Figure 13 - Carbon substrate utilisation (as percentage of the total) determined in the epi-, meso-, and bathy-pelagic layers.

Enzymatic activity measurements yield values of LAP, GLU and AP ranging from 0.072 to 8.08 nM h^{-1}, from 0.007 to 0.35 nM h^{-1} and from 0.001 to 0.36 nM h^{-1} respectively (Fig. 14). Total enzymatic patterns depict vertical trends generally decreasing from surface towards deep layers, with some hot spots of metabolic activity at 20-40 m and in the aphotic layer. LAP activity peaks at the lateral ends of the transect as well as at st. 20. AP and GLU decrease from the Western (Greenland) side moving towards St 20, then increase again towards the Eastern side (st. 10) of the transect.

548
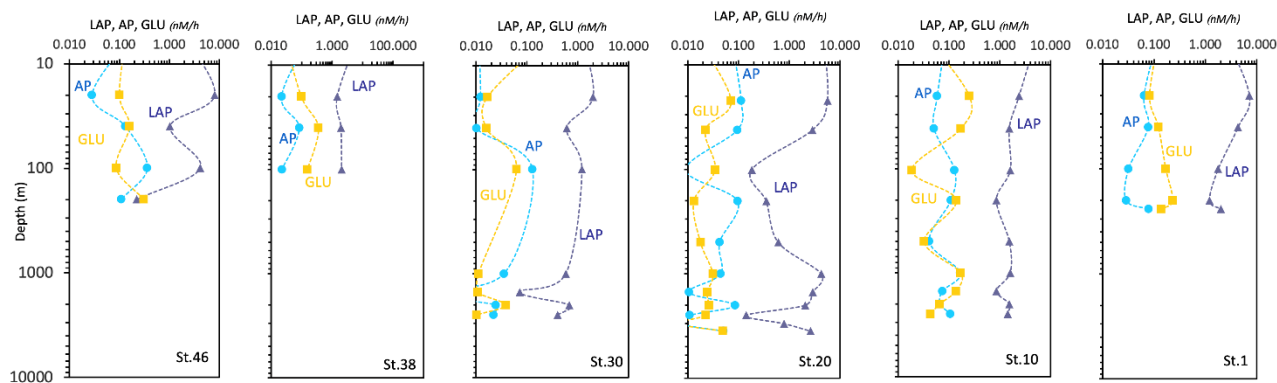
549 **Figure 14** - Vertical profiles of the enzymatic activity rates measured at the sampled stations (LAP, leucine
550 aminopeptidase; AP, alkaline phosphatase; GLU, beta glucosidase). Data are represented in natural log (*ln)* scale.

551

552 The respiration rates (ETS) range from 0.0290 to 0.329 μL O_2 h^{-1} L^{-1} (Fig. 15). The respiratory
553 activity values generally decrease from the surface down to 1000 m depth and then increase again
554 in the deep layer (below 1000 m depth). A high value of respiratory activity was also determined
555 in the deepest sample of st. 46.

556
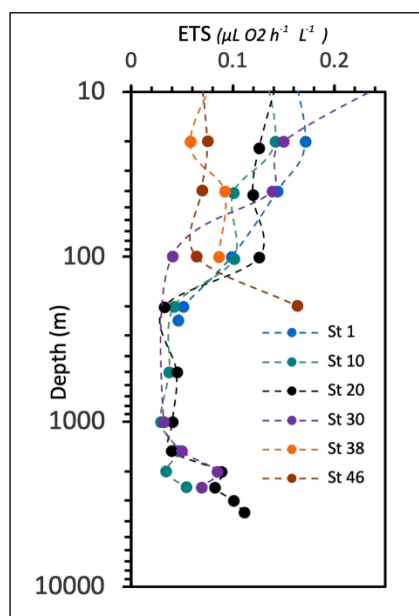
557 **Figure 15** - Vertical profiles of Electron Transport System (ETS) respiratory activity. Data on the y axis are
558 represented in natural log (*ln)* scale.

559

4   Summary and conclusions

Here we present the main data and results of the multidisciplinary oceanographic campaign carried out between 29 August and 14 September 2021 on board the Italian icebreaker Laura Bassi in the Greenland Sea (along the 75° N latitude section) as part of the Italian project CASSANDRA, funded by the Italian Ministry of Research in the framework of the Italian Arctic Programme. The Greenland Sea, in the north Atlantic, is a region of deep ocean convection that contributes to the AMOC and the exchange of water masses between the Atlantic and Arctic Oceans. On its easternmost side, it is dominated by the presence of AW, while on the westernmost side, by the presence of Polar waters. Both large scale patterns, local meteorological conditions, and ice extent can influence physical and biogeochemical properties. Different phases of the North Atlantic Oscillation index (NAO, i.e., atmospheric pressure difference between the Azores high and the subpolar low at sea level) can modulate basin-wide changes in the intensity and position of the North Atlantic jet stream and storm track, as well as influence patterns of zonal and meridional heat and moisture transport, which in turn can affect temperature and precipitation patterns over the Arctic and sub-Arctic regions. Increasingly positive phases of the NAO are associated with increased AW inflow, as was the case in the late 1980s/early 1990s (Dickson et al., 2000). The winter of 2020/2021, which preceded the cruise, had a slightly negative NAO index (-0.72), after two years of predominantly positive values. A negative NAO means weaker westerly winds in the mid-latitude regions in terms of climatology and stronger winds in the North Atlantic west of Iceland. Sea ice in the Fram Strait fluctuates from year to year. The lowest extent in September was recorded exactly in 2021, the highest in 1987. In the long term, the regions of the Norwegian Sea and the Fram Strait experienced a drop in temperature from 2018 to 2020, which rose again in 2021. Instead, a strong freshening phase set in after 2013, which is continuing. Continuous warming was also observed in the deep-water layer of the Greenland Sea at a depth of 3000 metres. In particular, the GSDW temperature shows a relatively steady increase from -1.18 °C to -0.86 °C between 1993 and 2021 (ICES Report on Ocean Climate 2021, available at https://ices-library.figshare.com/articles/report/ICES_Report_on_Ocean_Climate_2021/24755574?file=43769571). Our measurements report temperature values of about -0.9 °C for the GSDW. Relatively warm and saline Atlantic Water (AW, $\theta > 3.0°C$, S about 35), with highest A_T concentrations, dominates on the eastern side in the upper 500 m with surface temperatures of 4.5–9.0 °C. A dome-shaped isotherm distribution indicates upwelling from the Greenland Sea Gyre, while several mesoscale structures such as eddies seem to be responsible for the large spatial variability in the upper layer. At the surface, the central Greenland Sea is almost nutrient poor. On the western side, however, higher phosphate and silicate values are good indicators for the upper halocline of the Arctic surface water along the Greenland slope. Nitrate levels remained very low there. The deep waters NSDW and GSDW, presented the lowest pH_T values and the highest enrichment of silicate. Phytoplankton biomass along the euphotic water column, expressed as chl-*a*, showed a difference between the central-eastern and western sectors with greater abundances at the extremes of the transect. The dimensional structure of the phytoplankton community characterizes the PW with a predominance of the micro-phytoplankton fraction that almost entirely replaces the nano-phytoplankton fraction, more abundant in the AW, even in the front station between these two water masses. The plankton communities were analysed with more detail in the upper layer (0-100 m), where the phytoplankton and zooplankton diversity reflected the different water masses (AW and PW). Diatoms increased at the western stations affected by PW, while dinoflagellates and small flagellates were more abundant

at the eastern stations affected by AW. The higher MZP abundance was recorded at st. 38, where the layer below 30-40 m depth was still occupied by AW, while the surface layer was affected by PW. The MZP abundance and biomass decreased drastically in the presence of cold PW on the Greenland slope. Micrometazoans and aloricate ciliates increased towards the easternmost side of the section, where the stations were characterised by higher sea temperatures. Copepods of the genus *Calanus* were the main taxa observed, but the structure of the mesozooplankton communities changed along the transect and polar taxa increased westwards. The δ^{18}O and δD isotope ratios indicate the influence of freshwater at the surface level near the Greenland shelf. We also highlight a marked difference in δ^{18}O and δD isotope ratios between GSDW and NSDW, which occupies the bottom region of the studied area, with NSDW showing lower values compared to GSDW. Prokaryotic abundance and microbial enzymes generally depicted vertical decreasing trends with peaks of cells and activity recorded at station 20 as well as at the ends of the transect. While living cells prevailed at station 46 in the photic layer, actively respiring cells were quite variable in their distribution. Large, curved rods were found at stations 30 and 10. A high utilisation of carbohydrates and carboxylic acids regardless of the examined station or depth characterized the microbial community metabolism. Amino acids were actively metabolised in the aphotic layer, while no differences were found in the utilisation of complex carbon sources and phosphate carbon compounds along the water column.

This study emphasises the significant spatial and vertical variability of water properties, nutrient distribution and biological communities caused by local and seasonal oceanographic dynamics in a region characterised by a strong exchange of water masses between the Arctic and Atlantic Oceans and a major influence of atmospheric teleconnections between the polar and subpolar regions.

5 Data availability

Data presented here are available through the repository Italian Arctic Data Center (IADC), at the following links: CTD casts, available at https://doi.datacite.org/dois/10.71761%2Fc082c3ca-40bf-42b1-a61a-7b3697ab2c5a (Bensi et al., 2024). Physical, biological, and biogeochemical analyses on water samples from Niskin bottles available at https://doi.datacite.org/dois/10.71761%2Ff7474404-3331-43e5-883b-25755e94956d (Azzaro et al., 2024). Satellite data used in the work are freely available at https://worldview.earthdata.nasa.gov/. Data on sea ice extension are available at https://mosj.no/en/indikator/climate/ocean/sea-ice-extent-in-the-barents-sea-and-fram-strait/.

Declaration of Competing Interest

The authors declare that they have no known competing financial interests or personal relationships that could have appeared to influence the work reported in this paper.

Acknowledgements

The field activities carried out on board the icebreaker Laura Bassi were partly funded by the Italian Ministry of University and Research through the Italian Arctic Research Programme (https://www.programmaricercaartico.it/), the National Institute of Oceanography and Applied Geophysics (OGS), and the National Research Council (CNR). The research was conducted as part of the project "AdvanCing knowledge on the presentArctic Oceanby chemical-phySical,

644 biogeochemical and biological obServAtioNs to preDict the futuRe chAnges" (CASSANDRA),
645 which was funded by the Italian Arctic Research Programme (PRA21_0001). This study was
646 partially funded by the project PRIN 2022/2022CCRN7R - "ATTRACTION" and supported by the
647 Synoptic Arctic Survey (SAS) – an international research programme that coordinates the data
648 collection of essential ocean variables measured during Arctic research cruises. SAS is partly
649 funded by the European Union's Horizon 2020 research and innovation programme through the
650 Arctic PASSION project under the grant agreement 10100347. We would like to thank Lidia Urbini,
651 Paolo Mansutti (OGS, Italy) Leonardo Langone, Patrizia Giordano, Warren Cairns (CNR-ISP,
652 Italy), Matteo Feltracco (UNIVE, Italy), the entire technical staff of the OGS, the captain and crew
653 of the Laura Bassi for their support during the data collection. We also thank Alenka Goruppi and
654 Giulia Peloso (OGS, Italy) for their help in processing the zooplankton data and Nives Ogrinc (Jožef
655 Stefan Institute Ljubljana, Slovenia) for the analyses of δ13C-DIC.

Author contribution

657 M.B., M.A. and G.Ci. conceived and wrote the main part of the article. M.B., M.A., G.Ci., M.G.,
658 V.K., C.R, M.M, T.D., F.R., M.K., A.L.G., V.T., E.P., A.d.O., D.B., F.C., A.C.R., M.P., G.Ca.,
659 G.M., C.T., L.P. F.S., F.D., C.C. contributed to the collection and/or processing of the data,
660 preparation of figures, and to the discussion of the results. M.A. led the CASSANDRA project. All
661 authors have contributed to the preparation and revision of the final version of the manuscript.

References

Ahme, A., Von Jackowski, A., McPherson, R. A., Wolf, K. K. E., Hoppmann, M., Neuhaus, S. and John, U.: Winners and Losers of Atlantification: The Degree of Ocean Warming Affects the Structure of Arctic Microbial Communities, Genes, 14, 623. https://doi.org/10.3390/genes14030623, 2023.

Andersen, P., and Throndsen, J.: Estimating cell numbers, in: Manual on Harmful Marine Microalgae, edited by: Hallegraeff, G. M., Anderson, D. M., and Cembella, A., Monographs on Oceanographic Methodology, Unesco Publishing, Paris, France, 11, 99–130, 2004.

Anderson, L. G., Drange, H., Chierici, M., Fransson, A., Johannessen, T., Skjelvan, I., and Rey, F.: Annual carbon fluxes in the upper Greenland Sea based on measurements and a box-model approach. Tellus, 52B, 1013-1024, 2000.

Azzaro, M., Specchiulli, A., Maimone, G., Azzaro, F., Lo Giudice, A., Papale, M., La Ferla, R., Paranhos, R., Souza Cabral, A., Rappazzo, A. C., et al.: Trophic and Microbial Patterns in the Ross Sea Area (Antarctica): Spatial Variability during the Summer Season. J. Mar. Sci. Eng. 10, 1666. https://doi.org/ 10.3390/jmse10111666, 2022.

Azzaro M., Aliani S., Maimone, G., Decembrini F., Caroppo C., Giglio F., Langone L., Miserocchi S., Cosenza A., Azzaro F., et al.: Short-term dynamics of nutrients, planktonic abundances and microbial respiratory activity in the Arctic Kongsfjorden (Svalbard, Norway), Polar Biol. 44, 361–378, 2021.

Azzaro, M., Bensi, M., Civitarese, G., et al: CTD (data from NISKIN Bottles) LB21 ARCTIC Cruise Italian Arctic project CASSANDRA [Data set], ISP-CNR. https://doi.org/10.71761/F7474404-3331-43E5-883B-25755E94956D, 2024.

Azzaro, M., La Ferla, R., and Azzaro, F.: Microbial respiration in the aphotic zone of the Ross Sea (Antarctica), Mar. Chem., 99(1), 199-209, https://doi.org/ 10.1016/j.marchem.2005.09.011, 2006.

Babb, D. G., Galley, R. J., Kirillov, S., Landy, J. C., Howell, S. E. L., Stroeve, J. C., Meier, W., Ehn, J. K., and Barber, D. G.: The stepwise reduction of multiyear sea ice area in the Arctic Ocean since 1980, J. Geophys. Res. Oceans, 128, 10, https://doi.org/10.1029/2023JC020157, 2023.

Beers, J. R., and Stewart, G. L.: Numerical abundance and estimated biomass of microzooplankton, in: The ecology of the plankton off La Jolla, California, in the period April through September 1967, edited by: Strickland, J. D. H., University of California Press, Berkeley, USA, 67–87, 1970.

Bensi, M., Kovacevic, V., & Mansutti, P.: CTD (DOWNCAST) LB21 ARCTIC Cruise Italian Arctic project CASSANDRA [Data set], IADC. https://doi.org/10.71761/C082C3CA-40BF-42B1-A61A-7B3697AB2C5A, 2024.

Brakstad, A., Våge, K., Håvik, L., and Moore, G. W. K.: Water Mass Transformation in the Greenland Sea during the Period 1986–2016, J. Phys. Oceanogr., 49, 121–140, https://doi.org/10.1175/JPO-D-17-0273.1, 2019.

Carmack, E., Polyakov, I., Padman, L., Fer, I., Hunke, E., Hutchings, J., Jackson, J., Kelley, D., Kwok, R., Layton, C., Melling, H., Perovich, D., Persson, O., Ruddick, B., Timmermans, M., Toole, J., Ross, T., Vavrus, S., and Winsor, P.: Toward Quantifying the Increasing Role of Oceanic Heat in Sea Ice Loss in the New Arctic, Bull. of the Am. Met. Society, 96(12), 2079-2105, https://doi.org/10.1175/BAMS-D-13-00177.1, 2015.

Carpenter, J. H.: The accuracy of the Winkler method for dissolved oxygen analysis. Limnol. Oceanogr., 10, 135–140, https://doi.org/10.4319/lo.1965.10.1.0135, 1965.

Carter-Gates, M., Balestreri, C., Thorpe, S. E., Cottier, F., Baylay, A., Bibby, T. S., et al.: Implications of increasing Atlantic influence for Arctic microbial community structure, Sci. Rep., 10, 19262, https://doi.org/10.1038/s41598-020-76293-x, 2020.

Caruso, G., La Ferla, R., Azzaro, M., Zoppini, A., Marino, G., Petochi, T., et al.: Microbial assemblages for environmental quality assessment: knowledge, gaps and usefulness in the European Marine Strategy Framework Directive, Crit. Rev. Microbiol., 42, 883–904, https://doi.org/10.3109/1040841X.2015.1087380, 2016.

Caruso, G., Madonia, A., Bonamano, S., Miserocchi, S., Giglio, F., Maimone, G., et al.: Microbial abundance and enzyme activity patterns: response to changing environmental characteristics along a transect in Kongsfjorden (Svalbard Islands), J. Mar. Sci. Eng., 8, 824, https://doi.org/10.3390/jmse8100824, 2020.

Chatterjee, S., Raj, R. P., Bertino, L., Skagseth, Ø., Ravichandran, M., and Johannessen, O. M.: Role of Greenland Sea Gyre Circulation on Atlantic Water Temperature Variability in the Fram Strait, Geophys. Res. Lett., 45, 8399–8406, https://doi.org/10.1029/2018GL079174, 2018.

Clarke, R., Swift, J., Reid, J., and Koltermann, K.: The formation of Greenland Sea Deep Water: double diffusion or deep convection? Deep Sea Res. Part A, Oceanogr. Res. Pap., 37, 1385-1424 https://doi.org/10.1016/0198-0149(90)90135-I, 1990.

Csapó, H. R., Grabowski, M., and Węsławski J.M.K.: Coming home - Boreal ecosystem claims Atlantic sector of the Arctic, Sci. Total Environ., 771, 144817, https://doi.org/10.1016/j.scitotenv.2020.144817, 2021.

Decembrini, F., Caroppo C., Caruso, G., and Bergamasco, A.: Linking microbial functioning and trophic pathways to mesoscale processes and ecological status in a coastal ecosystem: Gulf of Manfredonia (south Adriatic Sea), Water, 13, 1325. https://doi.org/10.3390/w13091325, 2021.

Dickson, R. R., Osborn, T. J., Hurrell, J. W., Meincke, J., Blindheim, J., Adlandsvik, B., et al.: The Arctic Ocean Response to the North Atlantic Oscillation, J. Climate, 13, 2671–2696, https://doi.org/10.1175/1520-0442(2000)013<2671:TAORTT>2.0.CO;2, 2000.

734 de Steur, L., Sumata, H., Divine, D. V., et al.: Upper ocean warming and sea ice reduction in the
735   East Greenland Current from 2003 to 2019, Commun. Earth Environ. 4, 261,
736   https://doi.org/10.1038/s43247-023-00913-3, 2023.

737 Dukhovskoy, D. S., Yashayaev, I., Proshutinsky, A., Bamber, J. L., Bashmachnikov, I. L.,
738   Chassignet, E. P., et al.: Role of Greenland freshwater anomaly in the recent freshening of the
739   subpolar North Atlantic. J. Geophys. Res. Oceans, 124, 3333–3360,
740   https://doi.org/10.1029/2018JC014686, 2019.

741 Edler, L.: Recommendations for marine biological studies in the Baltic Sea. Phytoplankton and
742   chlorophyll. Baltic Mar. Biol., 5, 1-37, 1979.

743 Fan, H., Borchert, L.F., Brune, S., Koul, V., and Baehr, J.: North Atlantic subpolar gyre provides
744   downstream ocean predictability, npj Clim. Atmos. Sci., 6, 145, https://doi.org/10.1038/s41612-
745   023-00469-1, 2023.

746 Fransner F., Fröb F., Tjiputra J. , Goris N., Lauvset S. K., Skjelvan I., Jeansson E., Omar A., Chierici
747   M., Jones E., Fransson A., Ólafsdóttir S. R., Johannessen T., Olsen A.: Acidification of the
748   Nordic Seas, Biogeosciences, 19, 979–1012, https://doi.org/10.5194/bg-19-979-2022, 2022.

749 Grasshoff, K., Kremling, K., and Ehrhardt, M.: Methods of Seawater Analysis, Wiley-VCH,
750   Weinheim, 600 pp., 1999.

751 Hansen, H. P., and Koroleff, F.: Determination of nutrients, in: Methods of Seawater Analysis, 3rd
752   Edn., edited by: Grasshoff, K., Kremling, K., and Ehrhardt, M., Wiley-VCH, Weinheim, 159–
753   228, https://doi.org/10.1002/9783527613984.ch10, 1999.

754 Hoppe, H. G.: Use of fluorogenic model substrates for extracellular enzyme activity (EEA)
755   measurement of bacteria, 1st edition, In: Handbook of methods in aquatic microbial ecology,
756   edited by: Kemp, P. F., Sherr, B. F., Sherr, E. B., and Cole, J. J., Lewis Publisher, Boca Raton,
757   FL-USA, 423-432, https://doi.org/10.1201/9780203752746, 1993.

758 Ingrosso, G., Giani, M., Comici, C., Kralj, M., Piacentino, S., De Vittor, C., and Del Negro, P.:
759   Drivers of the carbonate system seasonal variations in a Mediterranean gulf, Estuar. Coast. Shelf
760   Sci. 168, 58-70, https://doi.org/10.1016/j.ecss.2015.11.001, 2016a.

761 Ingrosso, G., Giani, M., Cibic, T., Karuza, A., Kralj, M., and Del Negro, P.: Carbonate chemistry
762   dynamics and biological processes along a river–sea gradient (Gulf of Trieste, northern Adriatic
763   Sea), J.Mar. Syst. 155, 35–49. http://dx.doi.org/10.1016/j.jmarsys.2015.10.013, 2016b.

764 Ingvaldsen, R. B., Assmann, K. M., Primicerio, R., et al.: Physical manifestations and ecological
765   implications of Arctic Atlantification, Nat. Rev. Earth Environ. 2, 874–889,
766   https://doi.org/10.1038/s43017-021-00228-x, 2021.

767 La Ferla, R., Maimone, G., Azzaro, M., Conversano, F., Brunet, C., Cabral, A.S., and Paranhos, R.:
768   Vertical distribution of the prokaryotic cell size in the Mediterranean Sea, Helgol. Mar. Res. 66,
769   635–650, https://doi.org/10.1007/s10152-012-0297-0, 2012.

Noji, T. T., Rey, F., Miller, L. A., Borsheim, K. Y., and Urban-Rich, J.: Fate of biogenic carbon in the upper 200 m of the central Greenland Sea, Deep-Sea Res. II 46, 1497-1509, https://doi.org/10.1016/S0967-0645(99)00032-6, 1999.

Norwegian Polar Institute: Sea ice extent in the Fram Strait in September. Environmental monitoring of Svalbard and Jan Mayen (MOSJ). URL: http://mosj.no/en/climate/ocean/sea-ice-extent-barents-sea-fram-strait.html (https://mosj.no), 2022.

Onarheim, I. H., Årthun, M., Teigen, S. H., Eik, K. J., and Steele, M.: Recent Thickening of the Barents Sea ice cover, GRL, 51, e2024GL108225, https://doi.org/10.1029/2024GL108225, 2024.

Oudot, C., Gerard, R., Morin, P., and Gningue, I.: Precise shipboard determination of dissolved oxygen (Winkler procedure) for productivity studies with commercial system, Limnol. Oceanogr. 33, 146–150, ,https://doi.org/10.4319/lo.1988.33.6part2.1646, 1998.

Pettine, M., Capri, S., Manganelli, M., Patrolecco, L., Puddu, A., and Zoppini, A.: The Dynamics of DOM in the Northern Adriatic Sea. Estuar. Coast. Shelf Sci., 52, 471–489, https://doi.org/10.1006/ecss.2000.0752, 2001.

Polyakov, I. V., Ingvaldsen, R. B., Pnyushkov, A. V., Bhatt, U. S., Francis, J. A., and Janout, M., et al.: Fluctuating Atlantic inflows modulate Arctic Atlantification, Science, 381, 972-979, https://doi.org/10.1126/science.adh5158, 2023.

Polyakov, I. V., et al.: Greater role for Atlantic inflows on sea-ice loss in the Eurasian Basin of the Arctic Ocean. Science 356, 285-29 1, DOI:10.1126/science.aai8204, 2017.

Postel, L., Fock, H., and Hagen, W.: Biomass and abundance, ICES Zooplankton Meth. Manual, 83–192, https://doi.org/10.1016/B978-012327645-2/50005-0, 2000.

Priest, T., von Appen, WJ., Oldenburg, E., Popa, O., Torre-Valdés, S., Bienhold, C., et al.: Atlantic water influx and sea-ice cover drive taxonomic and functional shifts in Arctic marine bacterial communities, ISME J., 17, 1612–1625, https://doi.org/10.1038/s41396-023-01461-6, 2023.

Putt, M., and Stoecker, D. K.: An experimentally determined carbon: volume ratio for marine "oligotrichous" ciliates from estuarine and coastal waters, Limnol. Oceanogr., 34, 1097-1107, https://doi.org/10.4319/lo.1989.34.6.1097, 1989.

Rantanen, M., Karpechko, A.Y., Lipponen, A., et al.: The Arctic has warmed nearly four times faster than the globe since 1979, Commun. Earth Environ. 3, 168, https://doi.org/10.1038/s43247-022-00498-3, 2022.

Relitti, F., Ogrinc, N., Giani, M., Cerino, F., Smodlaka Tankovic, M., Baricevic, A., Urbini, L., Krajnc B., Del Negro, P., and De Vittor, C.: Stable carbon isotopes of phytoplankton as a tool to monitor anthropogenic CO_2 submarine leakages, Water, 12, 3573. https://doi.org/10.3390/w12123573, 2020.

Rudels, B., Friedrich, H. J., and Quadfasel, D.: The Arctic Circumpolar Boundary Current, Deep-Sea Res. Part II, 46, 1023-1062, https://doi.org/10.1016/S0967-0645(99)00015-6, 1999.

Schlitzer, R.: Ocean Data View, https://odv.awi.de, 2024.

Simpkins, G.: Greenland Sea convection, Nature Clim. Change 9, 7, https://doi.org/10.1038/s41558-018-0384-6, 2019.

Skjelvan, I., Olsen, A., Anderson, L. G., Bellerby, R. G. J., Falck, E, Kasajima, Y., Kivimäe, C., Abdirahman, O., Rey, F., Olsson, K. A., Johannessen, T., and Heinze, C.: A review of the inorganic carbon cycle of the Nordic Seas and Barents Sea. In: Drange H. et al. (Eds.) The Nordic Seas: An Integrated Perspective Oceanography, Climatology, Biogeochemistry, and Modeling., Geophys. Monogr. Ser., vol. 158, pp. 157-175, AGU, Washington, D. C. 2005.

Smedsrud, L. H., Muilwijk, M., Brakstad, A., Madonna, E., Lauvset, S. K., Spensberger, C., et al.: Nordic Seas Heat Loss, Atlantic Inflow, and Arctic Sea Ice Cover Over the Last Century, Rev. Geophys., 60, https://doi.org/10.1029/2020RG000725, 2022.

Throndsen, J.: Preservation and Storage, in: Phytoplankton Manual, edited by: Sournia, A., Unesco Publishing, Paris, France, 69–74, 1978.

Urbini, L., Ingrosso, G., Djakovac, T., Piacentino, S., and Giani, M.: Temporal and Spatial Variability of the CO_2 System in a Riverine Influenced Area of the Mediterranean Sea, the Northern Adriatic, Front. Mar. Sci., 679, https://doi.org/10.3389/fmars.2020.00679, 2020.

Utermöhl, H.: Zur Vervollkommung der quantitativen Phytoplankton-Methodik, Mitt Int Ver Theor Angew Limn, 9, 1-38, 1958.

van Guelpen, L., Markle, D. F., and Duggan, D. J.: An evaluation of accuracy, precision, and speed of several zooplankton subsampling techniques, ICES J. Mar. Sci., 40, 226–236, https://doi.org/10.1093/icesjms/40.3.226, 1982.

Verity, P. G., and Lagdon, C.: Relationship between lorica volume, carbon, nitrogen, and ATP content of tintinnids in Narragansett Bay, J. Plankton Res., 6, 859-868, https://doi.org/10.1093/plankt/6.5.859, 1984.

von Bodungen, B., Antia, A., Bauerfeind, E., et al.: Pelagic processes and vertical flux of particles: an overview of a long-term comparative study in the Norwegian Sea and Greenland Sea, Geol. Rundsch. 84, 11–27, https://doi.org/10.1007/BF00192239, 1995.

Wang, X., Zhao, J., Hattermann, T., Lin, L., and Chen, P.: Transports and accumulations of Greenland Sea intermediate waters in the Norwegian Sea, J. Geophys. Res.: Oceans, 126, e2020JC016582, https:// doi.org/10.1029/2020JC016582, 2021.

Whitt, D. B.: Global Warming Increases Interannual and Multidecadal Variability of Subarctic Atlantic Nutrients and Biological Production in the CESM1-LE, Geophys. Res. Lett., 50, https://doi.org/10.1029/2023GL104272, 2023.

840 Yergeau, E., Michel, C., Tremblay, J., Niemi, A., King, T. L., Wyglinski, J., et al.: Metagenomic
841   survey of the taxonomic and functional microbial communities of seawater and sea ice from the
842   Canadian Arctic, 10.1038/srep42242, Sci. Rep., 7, 42242, 2017.

843 Zingone., A., Totti, C., Sarno, D., Cabrini, M., Caroppo, C., Giacobbe, M. G., Lugliè, A., Nuccio,
844   C., and Socal, G. Fitoplancton: metodiche di analisi quali-quantitativa, in: Metodologie di studio
845   del plancton marino, edited by: Socal, G., Buttino, I., Cabrini, M., Mangoni, O., Penna, A., and
846   Totti, C., Manuali e Linee Guida ISPRA SIBM, Rome, Italy, 213–237, 2010.